

UNIVERSITY OF CINCINNATI

DATE: August 15, 2002

I, Lishan You,
hereby submit this as part of the requirements for the
degree of:

MASTER OF SCIENCE

in:

the Department of Mechanical, Industrial and
Nuclear Engineering

It is entitled:

Computational Modeling of Laminar Swirl Flows and
Heat Transfer in Circular Tubes with Twisted-Tape
Inserts

Approved by:

Raj M. Manglik

Milind A. Jog

Rupak K. Banerjee

Computational Modeling of Laminar Swirl Flows and Heat Transfer in
Circular Tubes with Twisted-Tape Inserts

A thesis submitted to the

Division of Research and Advanced Studies

of the University of Cincinnati

in partial fulfillment of the
requirements for the degree of

MASTER OF SCIENCE

in the Department of Mechanical, Industrial and Nuclear Engineering

of the College of Engineering

2002

by

Lishan You

B.S., Tsinghua University, China, 1996

Thesis Advisor and Committee Chair: Dr. Raj M. Manglik

ABSTRACT

A numerical study is carried out to predict the velocity and temperature distributions in fully developed, constant property, laminar flows in tubes containing twisted-tape inserts. The tape inserts are characterized by the twist ratio y (ratio of 180° twist pitch of the tape H to the tube inner diameter d), and the ratio of tape thickness δ to the tube diameter, δ/d . The swirl flow is simulated by following the helically twisted flow path in the partitioned tube represented by a semi-circular cross-section geometry. In this model, the tape thickness is neglected ($\delta = 0$), which is a reasonable first-order approximation as $\delta/d \sim O[10^{-2}]$ for most inserts used in practice.

For the numerical solution of the velocity problem, the stream function and vorticity formulation is employed. The corresponding non-linear governing differential equations for the stream function, vorticity, axial velocity and temperature distributions are discretized using the finite control-volume method. This procedure essentially retains the conservative forms of the governing equations, and provides second-order discretization accuracy for the numerical solution. For the heat transfer problem both the uniform wall temperature (UWT) and uniform heat flux (UHF) boundary conditions at the tube wall are considered. In addition, two variations of the tape surface condition are considered, namely, uniform temperature and zero heat flux. These two cases model the tape as having infinite and zero fin efficiency, respectively.

Results for the variations in the velocity and temperature fields with flow Reynolds number Re and tape twist ratio y are presented; the temperature distributions also reflects the

influence of fluid Prandtl number Pr . The twisted-tape induced swirl flow field is characterized by a single longitudinal vortex that breaks up into two counter-rotating helical vortices with increasing Re or decreasing y . Correspondingly, both the friction factor f and Nusselt number Nu increase substantially; in the case of heat transfer, Nusselt number also increases with Pr . The results for f and Nu are found to agree very well with the respective Manglik and Bergles (1993) correlations. This verifies the scaling of swirl flow effects by the parameter $Sw (= Re_s / \sqrt{y})$ as proposed by them.

ACKNOWLEDGEMENT

This research could not have been accomplished without the direction and inspiration of Professor Raj M. Manglik, my academic and research adviser. He recommended this topic to me, generously offered me his notes on the mathematical details of the problem, and spent a tremendous amount of his own time on this project. His interest, constructive guidance, and patient support are greatly appreciated. In one word, without his efforts to support this study, it would have never been started and successfully completed.

Additional help came from many other people and I am not able to list all of them by name. I am especially grateful to Alok Verma, who gave helpful advice on the discretization of the governing equations by using the Finite Control Volume Method. That made my task much easier. I also benefited from the discussions with Hossam Metwally and Dr. Pingping Fang. They provided, with sincerity, all they knew that was helpful to my study.

Finally, I would like to take this opportunity to also thank my thesis committee members, Professors Milind A. Jog and Rupak K. Banerjee, for their critical assistance.

TABLE OF CONTENTS

ABSTRACT	ii
ACKNOWLEDGEMENTS	v
LIST OF FIGURES	viii
LIST OF TABLES	ix
NOMENCLATURE	x
1 INTRODUCTION	1
1.1 Twisted_Tape Flow and Heat Transfer	2
1.2 Aim and Scope of the Study	7
2 TWISTED-TAPE GENERATED SWIRL FLOW CONVECTION	10
2.1 Physical Model	10
2.2 Mathematical Formulation	12
2.2.1 Helical coordinate system	15
2.2.2 Stream function and vorticity formulation	18
2.2.3 Dimensionless formulation	20
2.2.4 Generalized presentation of governing equations	21
2.3 Friction Factor and Nusselt Number	22
3 NUMERICAL SOLUTION	27
3.1 Finite Control Volume Method	29
3.2 Discretization of Governing Differential Equation	30
3.3 Solution Procedure	32
4 RESULTS AND DISCUSSIONS	36
4.1 Flow Field	36
4.1.1 Velocity distribution	37
4.1.2 Shear stress distribution	41
4.1.3 Friction factor	44
4.2 Heat Transfer	51
4.2.1 Temperature distribution	51
4.2.2 Nusselt number	56
5 CONCLUSIONS AND RECOMMENDATIONS	65
5.1 Conclusions	65
5.2 Recommendations	66

BIBLIOGRAPHY	67
Appendix A. Mean Velocity and Friction Factor	69
Appendix B. Mean Temperature and Nusselt Number	71
Appendix C. Discretization of Governing Equations	73
Appendix D. Convective, Diffusive, and Source Terms	78
Appendix E. Implementation of Boundary Conditions	80

LIST OF FIGURES

1.1 Shell-and-tube heat exchanger with twisted-tape inserts	3
1.2 Twisted-tape geometry	4
2.1 Representation of tube cross-section with a twisted-tape insert	11
2.2 Thermal boundary conditions	13
2.3 Coordinate systems	16
4.1 Effect of Re on the flow field for $y = 3$	39
4.2 Effect of y on the flow field for $Re = 800$	40
4.3 Shear stress distribution for $Re = 800$	42
4.4 Shear stress distribution for $y = 6$	43
4.5 Influence of the twist ratio y on friction factors	47
4.6 Comparison of the computational friction factor results with experimental data of Manglik and Bergles (1992)	48
4.7 Comparison of the computational fRe results with correlation of Manglik and Bergles (1993a)	50
4.8 Effect of Re on temperature distribution for $y = 3$ and $Pr = 1$	52
4.9 Effect of y on temperature distribution for $Re = 800$ and $Pr = 1$	54
4.10 Effect of Pr on temperature distribution for $y=6$ and $Re=600$	55
4.11 Influence of y on Nusselt numbers at $Pr = 1$ for Case 2 and UWT	60
4.12 Influence of Pr on Nusselt numbers at $y = 6$ for Case 2 and UWT	61
4.13 Comparison of Nu results with correlation of Manglik and Bergles (1993)	63
C.1 Finite Control Volume	74

LIST OF TABLES

2.1 Coefficients in general equations for ψ , ζ , w and T	21
2.2 Boundary conditions for ψ , ζ , w and T	22
4.1 Friction factors for different twist ratios (y) and flow rates (Re)	45
4.2 Nusselt numbers for Pr = 1 (Case 1)	59
4.3 Nusselt numbers for Pr = 1 (Case 2)	59
4.4 Nusselt numbers for Pr = 6 (Case 1)	60
4.5 Nusselt numbers for Pr = 6 (Case 2)	60
4.6 Nusselt numbers for Pr = 80 (Case 1)	61
4.7 Nusselt numbers for Pr = 80 (Case 2)	61

NOMENCLATURE

A	heat transfer area, m^2
A_c	flow area of cross-section, m^2
a_N, a_S, a_E, a_W, a_P	coefficients in the general discretized equation, Eq. (3.1) and (3.2)
b	integration of source term in the discretized equation, Eq. (3.1)
Br	Brinkman number, $= \mu V_a^2 / k\Delta T$
c_p	specific heat, $J / kg \cdot K$
d, D	tube inner diameter, m
d_h	hydraulic diameter, m
D_e, D_w, D_n, D_s	diffusive strengths, Eq. (3.2)
f	fanning friction factor based on tube inner diameter
F_e, F_w, F_n, F_s	convective strengths, Eq. (3.2)
G	dimensionless pressure drop constant, Eq. (2.17b)
Gz	Graetz number, $= \dot{m}c_p / kL$
h	heat transfer coefficient, $W / m^2 \cdot K$
H	pitch for 180° twist of tape, m
k	thermal conductivity of fluid, $W / m \cdot K$
L	axial length, m
\dot{m}	mass flow rate, kg / s
M	number of nodes in the angular direction
N	number of nodes in the radial direction

Nu	Nusselt number, $= h \cdot D / k$
p	pressure, Pa
Pe	Peclet number, $= V_a \cdot D / \alpha$
P_e, P_w, P_n, P_s	Pectlet number, Eq. (C.10)
P_w	peripheral length or wetted perimeter, m
Pr	Prandtl number, ν/α
\dot{q}	heat transfer rate, W
$\bar{r}, \bar{\theta}, \bar{z}$	stationary cylindrical coordinates, Fig. 2.3
r', θ', z'	helical coordinates, Fig. 2.3
r, θ, z	dimensionless helical coordinates, Eq. (2.16)
R	tube radius, m , Fig. 2.1
Ra	Rayleigh number, $= Gr \cdot Pr$
Re	Reynolds number based on tube inner diameter, $= V_a \cdot D / \nu$
Re_s	Reynolds number based on swirl velocity, $= V_s \cdot D / \nu$
RF	relaxation factor
S	source term, Eq. (2.19) and Table 2.1
Sw	swirl parameter, Eq. (1.2)
\bar{T}	temperature, K
T	dimensionless temperature, Eq. (2.17b)
$\bar{u}, \bar{v}, \bar{w}$	velocities, m/s
u, v, w	dimensionless velocities, Eqs. (2.17a) and (4.2)
V_a	mean axial velocity, m/s , Eq. (1.3b)

V_s	swirl velocity, m / s , Eq. (1.3b)
V_t	mean tangential velocity, m / s , Eq. (4.10)
\hat{w}	normalized axial velocity, $= w / G$
y	twist ratio, $= H / d$

Greek Symbols

α	thermal diffusivity, m^2 / s
β	coefficient of diffusive term with respect to θ in the general differential equation, Eq. (2.19)
Δ	distance between two faces of the control volume
δ	distance between two nodes, and tape thickness, Fig. 2.1
ε	relative error
ζ	dimensionless vorticity, Eq. (2.17a)
θ	angular coordinate
λ	coefficient of convective term with respect to r in the general differential equation, Eq. (2.19)
μ	coefficient of convective term with respect to θ in the general differential equation, Eq. (2.19)
ν	fluid kinetic viscosity, m^2 / s
ρ	fluid density, kg / m^3
ϕ	general function, Eq. (2.19)
ψ	dimensionless stream function, Eq. (2.17a)
τ	shear stress, Eq. (4.4)

Subscripts

b	bulk value
e, w, n, s	boundaries of the control volume in various directions
E, W, N, S	neighboring nodes
i	angular nodes index
j	radial nodes index
m	flow cross-section averaged or mean value
s	for swirl flows
w	at tube wall or tape surface
z	axially local value

CHAPTER 1. INTRODUCTION

Effective utilization, conservation, and recovery of heat are critical engineering problems for the process industry. The economic design and operation of process plants are often governed by the effective usage of heat. A majority of heat exchangers used in chemical, petrochemical, biomedical, and food processing plants serve to heat and cool viscous fluids. These activities involve multi-million dollar investments annually for both operation and capital costs. This is further compounded by the fact that viscous fluids are usually characterized by a low Reynolds number and laminar flow condition, whose heat transfer coefficient is relatively low and thus becomes the dominant thermal resistance in a heat exchanger. The adverse impact of low heat transfer coefficients of such flows on the size and cost of heat exchangers adds to excessive energy, material, and monetary expenditures.

The need to optimize and conserve these expenditures has promoted the development of more efficient heat exchangers. A variety of different techniques are employed for the heat transfer process, which is generally referred to as heat transfer *enhancement*, and extensive reviews of these methods and their applications have been given by Bergles (1998) and Webb (1994). These techniques are broadly classified as *active* or *passive* techniques. Passive techniques require no external energy input, except for pump or blower power to move the fluid, and involve the use of roughened surfaces, extended surfaces, displaced promoters, and swirl

flow devices, among some others. Active enhancement techniques, on the other hand, need extra power to effect the process to improve heat transfer. Consequently, passive techniques are often the preferred choice and they have seen wider applications.

Of the many enhancement techniques that can be employed, swirl flow generation by means of full-length twisted-tape inserts is found to be extremely effective (Bergles, 1998; Smithberg and Landis, 1964; Hong and Bergles, 1976; Date 1974; Manglik and Bergles, 1992, 2002; DuPlessis and Kröger, 1984, 1987). Significant heat transfer improvement can be obtained, particularly in laminar flows. Other examples of techniques that promote swirl flows include curved ducts, tangential fluid injection, and twisted or convoluted ducts. Their thermal-hydraulic characteristics, heat transfer improvement potential, and typical applications have been outlined by Nandakumar and Masliyah (1986), Bergles et al. (1991), Webb (1994) and Bergles (1998).

1.1 Twisted-Tape Flow and Heat Transfer

It is well known that energy transport is considerably improved if the flow is stirred and mixed well. This has been the underlying principle in the development of enhancement techniques that generate swirl flows. Among the techniques that promote secondary flows, twisted-tape inserts are perhaps the most convenient and effective (Manglik and Bergles, 2002). They are relatively easy to fabricate and fit in the tubes of shell-and-tube or tube-fin type heat exchangers. A typical usage in the multi-tube bundle of a shell-and-tube heat exchanger is shown in Fig. 1.1. The geometrical features of a twisted tape, as depicted in Fig. 1.2, are described by its 180° twist pitch H , the thickness δ , and the width w . In most usage, where snug-to-tight-fitting tapes are used, $w \cong d$, and the severity of the tape twist is characterized by the dimensionless

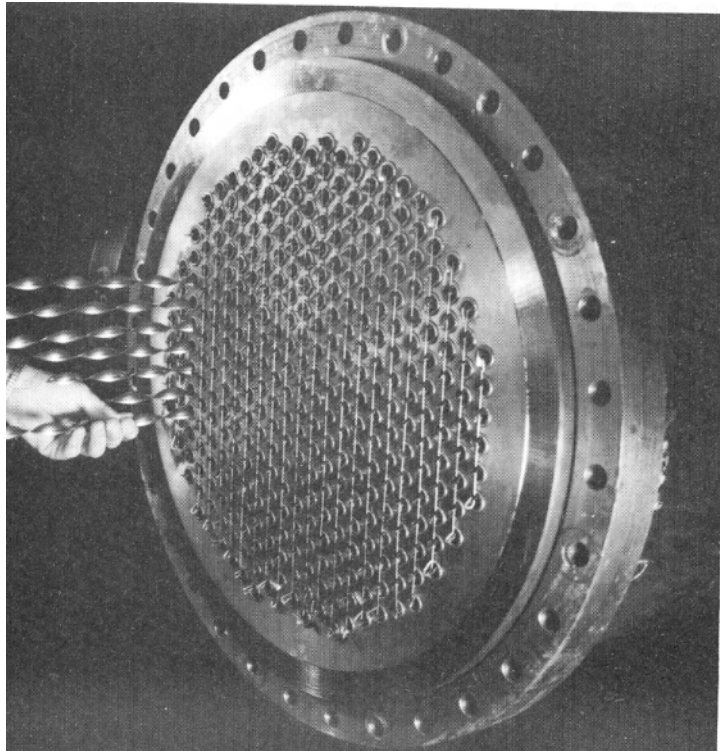


Fig. 1.1 Shell-and-tube heat exchanges with twisted-tape inserts

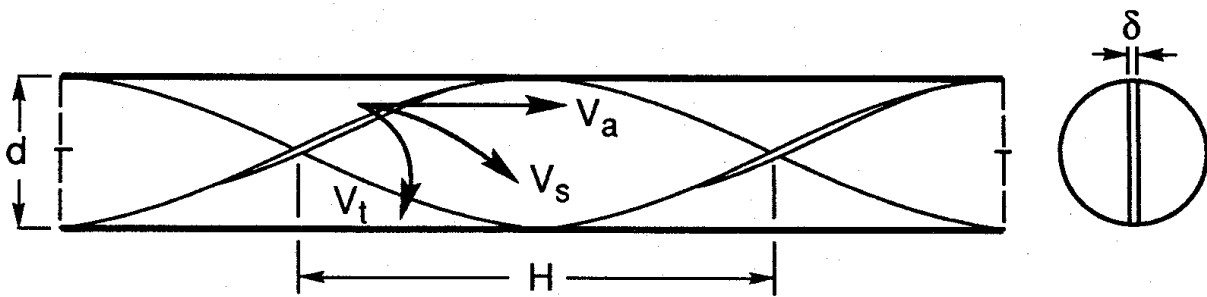


Fig. 1.2 Twisted-tape geometry

ratio $y = (H / d)$. The helical twisting nature of the tape, besides providing the fluid a longer flow path or a greater residence time, imposes a helical force on the bulk flow that promotes the generation of secondary circulation. The consequent well-mixed helical swirl flow significantly enhances the convective heat transfer (Manglik and Bergles, 2002, 1993a, 1993b). In most cases, depending on how tightly the tape fits at the tube wall and what material it is made of, there may be some tape-fin effects as well. The enhanced heat transfer due to twisted-tape inserts, is also accompanied by an increase in pressure drop and suitable trade-offs must be considered by designers to optimize their thermal-hydraulic performance.

Heat transfer enhancement in single-phase laminar flows has received considerable attention in the literature, as documented in a very recent and exhaustive survey by Manglik and Bergles (2002). Most of this work has been experimental, aimed at collecting pressure drop (friction factor) and heat transfer (Nusselt number) data, and characterizing their dependence on the geometry of the twisted-tape insert; see, for example, Hong and Bergles (1976), Marner and Bergles (1978, 1989), Manglik and Bergles (1992, 1993a). The fully developed swirl flow performance, in particular, has been found to be influenced by the severity of the tape's helical twist y , and its tube blockage factor (δ / d) , and the functional relationship can be expressed as

$$f = \phi(\text{Re}, y, \delta / d) \quad (1.1a)$$

$$Nu = \phi(\text{Re}, y, \delta / d, \text{Pr}) \quad (1.1b)$$

Many different correlations have been reported in the literature (see, for example, Hong and Bergles, 1976; Donevski and Kulesza, 1978; Watanabe et al., 1983; DuPlessis and Kröger, 1984, 1987; and others) to represent these relationships in laminar or low Reynolds number flows. The validity and applicability of these equations are discussed at length by Manglik and Bergles (1991, 1993a, 2002).

Based on a fundamental balance between inertia, viscous, and tape-geometry helical-curvature induced forces, Manglik and Bergles (1993a) have proposed that tape-induced swirl flows can be scaled by a swirl parameter defined as

$$Sw = Re_s / \sqrt{y} \quad (1.2)$$

where the swirl Reynolds number is based on the swirl velocity, and

$$Re_s = \rho V_s d / \mu \quad (1.3a)$$

$$V_s = V_a \left[1 + (\pi / 2y)^2 \right]^{1/2}, \quad V_a = \dot{m} / \rho A_c \quad (1.3b)$$

Correspondingly, they devised the following correlation to predict isothermal Fanning friction factors in the laminar flow regime:

$$(f Re)_s = 15.76 \left[\frac{\pi + 2 - 2\delta / d}{\pi - 4\delta / d} \right] \left(1 + 10^{-6} Sw^{2.55} \right)^{1/6} \quad (1.4)$$

This equation has been shown to predict very well (within $\pm 10\%$) the experimental data for f reported by several different investigations (Manglik and Bergles, 1993a; Manglik et al. 2001).

Furthermore, for laminar flow heat transfer in tubes subject to UWT conditions, Manglik and Bergles (1993a) have given the following mean or average Nusselt number correlation:

$$Nu_m = 4.612 \left(\frac{\mu_b}{\mu_w} \right)^{0.14} \left[\left\{ \left(1 + 0.0951 Gz^{0.894} \right)^{2.5} + 6.413 \times 10^{-9} (Sw \cdot Pr^{0.391})^{3.835} \right\} + 2.132 \times 10^{-14} (Re \cdot Ra)^{2.23} \right]^{0.1} \quad (1.5)$$

It may be noted that the uniform wall temperature (UWT) condition is frequently encountered in two-fluid process heat exchangers where the heating/cooling fluid undergoes phase change (condensation/boiling). For uniformly heated (UHF) tubes, the older Hong and Bergles (1976) correlation given below, which does not employ the swirl parameter, is often cited:

$$Nu_z = 5.172 \left[1 + 5.484 \times 10^{-3} Pr^{0.7} (Re / y)^{1.25} \right]^{1/2} \quad (1.6)$$

This equation, of course, correlates the axially local Nusselt number, rather than the mean value.

Few attempts have been made to characterize and understand the structure of twisted-tape-induced swirl flows. In perhaps the first and only such work for laminar flows, Manglik and Ranganathan (1997) have visualized the secondary flow patterns using smoke injection techniques. From their observations of a limited number of cases, they suggest a three-zone flow behavior: viscous-flow, no swirl regime; swirl-transition regime; and fully developed swirl-flow regime. The fully established swirl was found to consist of two dissimilar, counter-rotating, helical vortices. This latter structure had earlier been suggested by Seymour (1966) as well in another flow visualization study, but for turbulent flows.

Computational simulations are also very useful for determining the local flow and thermal characteristics. However, the reported numerical investigations (Date and Singham, 1972; Date, 1974; Duplessis and Kröger, 1984, 1987; Date, 2000) have primarily focussed on evaluating global thermal-hydraulic behavior (friction factor, Nusselt number and the relative heat transfer enhancement) rather than the structure of velocity and temperature fields. This is rather unfortunate, as computational techniques are ideally suited for extracting such information. Nevertheless, the axial velocity distributions presented by Date (1974), with two local peaks, implicitly suggest a double-vortex structure of fully developed swirl flows.

1.2 Aim and Scope of Study

The objective of this thesis is to investigate the swirl flow behavior and the laminar convective heat transfer in a circular tube with twisted-tape inserts. The fluid flow and thermal fields are simulated computationally in an effort to characterize their structure. The local wall shear stress and heat flux or temperature distributions are determined, along with the average friction factors and Nusselt numbers for different flow Reynolds numbers, twisted-tape

geometry, and wall thermal boundary conditions. Both the uniform wall temperature (UWT or T) and uniform wall heat flux (UHF or H) conditions are considered with two variations. Furthermore, the heat transfer results are obtained for different fluids that are represented by the Prandtl number range of $1 \leq Pr \leq 80$. The results highlight the influence of tape geometry and fluid flow conditions in promoting swirl flows and the consequent enhanced heat transfer. The nature of the swirl (or vortex structure) is delineated, and shown to corroborate the observations made in an earlier flow visualization experiment (Manglik and Ranganathan, 1997). Finally, the friction factor and Nusselt number results are compared with those predicted by the Manglik and Bergles (1993a) correlations, where the remarkable agreement is noted.

The mathematical formulation of the swirl-flow convection problem is described in Chapter 2. The governing equations for the momentum and energy transport are transformed in a helical coordinate system, which follows the path of a semi-circular channel that is axially twisting in a regular helix. For the velocity field, the stream function-vorticity formulation is outlined, so also the mathematical development for the local wall shear stress and heat transfer coefficient, and the average friction factor and Nusselt number.

The numerical methodology of the finite control volume technique, and the associated discretization of the governing equations are outlined in Chapter 3. It includes algorithm for obtaining computational solutions, and the selection and refinement of the grid.

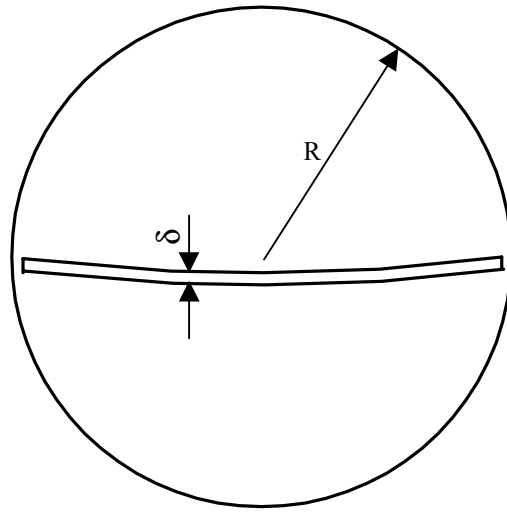
Chapter 4 has the presentation of results and their discussion. The velocity and temperature distributions, wall shear stress, and average friction factors and Nusselt numbers are presented, and their variations with the tape-twist ratio y , flow Reynolds number, and fluid Prandtl number (in the case of heat transfer) are delineated. Also the computational results are compared with experimental data and correlations.

Finally, the main conclusions drawn from the results of this computational study, and the recommendations for future work are outlined in Chapter 5.

CHAPTER 2. TWISTED-TAPE GENERATED SWIRL FLOW CONVECTION

2.1 Physical Model

A twisted-tape insert essentially partitions the tube into circular-segment flow cross sections with a helically twisting longitudinal path. Though the tape has a finite thickness, it is usually small ($\delta/d \sim O[10^{-2}]$; Manglik et al., 2001) and, to a good first-order approximation, can be ignored ($\delta \sim 0$). As such, swirl flows that are induced by twisted-tape inserts in straight circular tubes can be modeled by considering a semi-circular flow cross section with a regular helix twist geometry. This model also excludes the flow leakage from tape ends that might occur in snug-to-loose-fitting tapes that are commonly employed in practice; an extremely tight fit between the tape and the tube would eliminate the end leakage. Another simplification inherent in this model is that it ignores the small surface curvature that tapes have when fitted inside a tube in actual practice, and the two partitioned flow cross sections on either side of the tape are not symmetrically identical (Fig. 2.1(a)). These effects are, however, difficult to simulate, and the simplified physical representation shown in Fig. 2.1(b) provides a reasonable first-order computational model.



(a) Curved finite-thickness tape

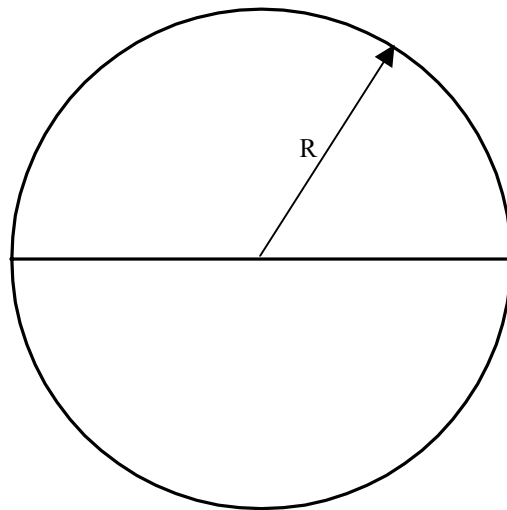


Fig. 2.1 Representation of tube cross-section with a twisted-tape insert:
(a) actual geometry; (b) simplified geometry for numerical solution

Besides the geometry of the flow model, another important aspect is the description of thermal boundary conditions that correspond to the heating/cooling load at the tube wall as well as the tape surface. Depending upon how the twisted-tape insert fits in the tube and its edge contact with the tube wall, the tape insert may have a significant fin effect. Complete modeling of the tape surface thermal conditions entails a rather complex problem with a conjugate treatment of the fin equation for the tape. However, the following two cases describe the extreme limits of the fin-effect:

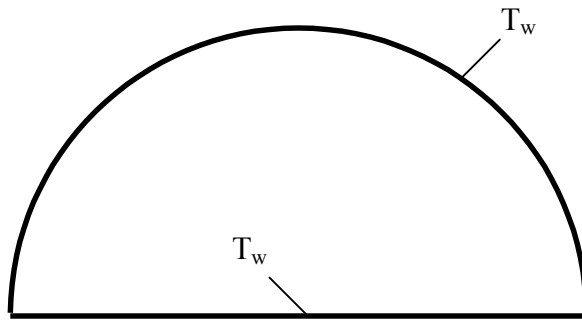
- (a) The tape surface is adiabatic, or has zero fin efficiency, i.e., the tape is either made of an insulating material or is in very poor thermal contact with the tube.
- (b) The tape surface is at the same temperature as the inside tube wall, i.e., it has 100% fin efficiency and is in very good thermal contact with the tube wall.

Furthermore, the tube wall itself could be at uniform wall temperature (UWT) or have a uniform wall heat flux (UHF) applied to it. The UWT condition, for example, simulates heating/cooling by steam condensation or refrigerant evaporation; the UHF condition models heating/cooling in a two-fluid heat exchanger with equal heat capacity rate flows. These boundary conditions are schematically shown in Fig. 2.2.

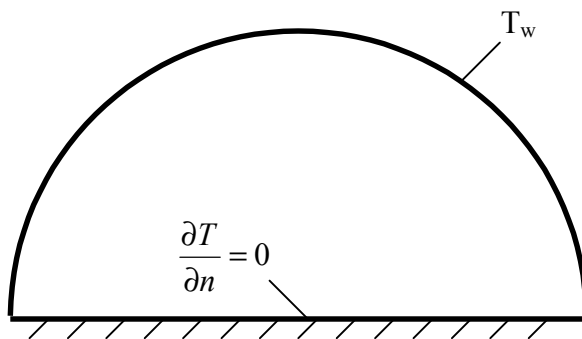
2.2 Mathematical Formulation

Steady, incompressible, fully developed laminar swirl flows are considered in this study, with the following simplifications:

- Newtonian fluid, having constant properties
- Negligible axial heat conduction ($Pe \gg 1$)
- Negligible viscous dissipation ($Br < 1$)



(a)



(b)

Fig. 2.2 Thermal boundary conditions: (a) Case 1; (b) Case 2

With these assumptions, the general transport equations for mass, momentum, and energy transportation,

$$\begin{aligned}
\text{Continuity:} \quad & \nabla \cdot \mathbf{V} = 0 \\
\text{Momentum:} \quad & \rho \mathbf{V} \cdot \nabla \mathbf{V} = -\nabla \mathbf{p} + \mu \nabla^2 \mathbf{V} \\
\text{Energy:} \quad & (\mathbf{V} \cdot \nabla) \bar{T} = \alpha \nabla^2 \bar{T}
\end{aligned} \tag{2.1}$$

can be cast in a cylindrical coordinate system $(\bar{r}, \bar{\theta}, \bar{z})$, shown in Fig.2.3, as follows:

Continuity:

$$\frac{\partial \bar{u}}{\partial \bar{r}} + \frac{\bar{u}}{\bar{r}} + \frac{1}{\bar{r}} \frac{\partial \bar{v}}{\partial \bar{\theta}} + \frac{\partial \bar{w}}{\partial \bar{z}} = 0 \tag{2.2a}$$

Axial momentum:

$$\begin{aligned}
\bar{u} \frac{\partial \bar{w}}{\partial \bar{r}} + \frac{\bar{v}}{\bar{r}} \frac{\partial \bar{w}}{\partial \bar{\theta}} + \bar{w} \frac{\partial \bar{w}}{\partial \bar{z}} = -\frac{1}{\rho} \frac{\partial \bar{p}}{\partial \bar{z}} + \\
\nu \left[\frac{\partial^2 \bar{w}}{\partial \bar{r}^2} + \frac{1}{\bar{r}} \frac{\partial \bar{w}}{\partial \bar{r}} + \frac{1}{\bar{r}^2} \frac{\partial^2 \bar{w}}{\partial \bar{\theta}^2} + \frac{\partial^2 \bar{w}}{\partial \bar{z}^2} \right]
\end{aligned} \tag{2.2b}$$

Radial momentum:

$$\begin{aligned}
\bar{u} \frac{\partial \bar{u}}{\partial \bar{r}} + \frac{\bar{v}}{\bar{r}} \frac{\partial \bar{u}}{\partial \bar{\theta}} - \frac{\bar{v}^2}{\bar{r}} + \bar{w} \frac{\partial \bar{u}}{\partial \bar{z}} = -\frac{1}{\rho} \frac{\partial \bar{p}}{\partial \bar{r}} + \\
\nu \left[\frac{\partial^2 \bar{u}}{\partial \bar{r}^2} + \frac{1}{\bar{r}} \frac{\partial \bar{u}}{\partial \bar{r}} + \frac{1}{\bar{r}^2} \frac{\partial^2 \bar{u}}{\partial \bar{\theta}^2} + \frac{\partial^2 \bar{u}}{\partial \bar{z}^2} - \frac{\bar{u}}{\bar{r}^2} - \frac{2}{\bar{r}^2} \frac{\partial \bar{v}}{\partial \bar{\theta}} \right]
\end{aligned} \tag{2.2c}$$

Angular momentum:

$$\begin{aligned}
\bar{u} \frac{\partial \bar{v}}{\partial \bar{r}} + \frac{\bar{v}}{\bar{r}} \frac{\partial \bar{v}}{\partial \bar{\theta}} + \frac{\bar{u}\bar{v}}{\bar{r}} + \bar{w} \frac{\partial \bar{v}}{\partial \bar{z}} = -\frac{1}{\rho} \frac{\partial \bar{p}}{\partial \bar{\theta}} + \\
\nu \left[\frac{\partial^2 \bar{v}}{\partial \bar{r}^2} + \frac{1}{\bar{r}} \frac{\partial \bar{v}}{\partial \bar{r}} + \frac{1}{\bar{r}^2} \frac{\partial^2 \bar{v}}{\partial \bar{\theta}^2} + \frac{\partial^2 \bar{v}}{\partial \bar{z}^2} - \frac{\bar{v}}{\bar{r}^2} + \frac{2}{\bar{r}^2} \frac{\partial \bar{u}}{\partial \bar{\theta}} \right]
\end{aligned} \tag{2.2d}$$

Energy:

$$\bar{u} \frac{\partial \bar{T}}{\partial \bar{r}} + \frac{\bar{v}}{\bar{r}} \frac{\partial \bar{T}}{\partial \bar{\theta}} + \bar{w} \frac{\partial \bar{T}}{\partial \bar{z}} = \alpha \left[\frac{\partial^2 \bar{T}}{\partial \bar{r}^2} + \frac{1}{\bar{r}} \frac{\partial \bar{T}}{\partial \bar{r}} + \frac{1}{\bar{r}^2} \frac{\partial^2 \bar{T}}{\partial \bar{\theta}^2} + \frac{\partial^2 \bar{T}}{\partial \bar{z}^2} \right] \tag{2.2e}$$

2.2.1 Helical coordinate system

The governing transport equations can be recast in a helical coordinate system (r', θ', z') , which takes the helical longitudinal path of the tape and where the angular coordinate is always measured from its surface. This coordinate system is defined relative to the stationary cylindrical coordinate system $(\bar{r}, \bar{\theta}, \bar{z})$ (see Fig. 2.3) as follows:

$$\begin{aligned} r' &= \bar{r} \\ \theta' &= \bar{\theta} + \frac{\pi \bar{z}}{H} \\ z' &= \bar{z} \end{aligned} \quad (2.3)$$

Here, the positive sign before the $(\pi \bar{z} / H)$ term implies anti-clockwise rotation of the tape as \bar{z} increases, when \bar{z} and z' are measured in the direction of the axial flow, and $\bar{\theta}$ and θ' are measured in the clockwise direction at the tape surface. By applying the chain rule, the following relations can then be written for the respective derivatives:

$$\begin{aligned} \frac{\partial}{\partial \bar{r}} &= \frac{\partial}{\partial r'} \\ \frac{\partial}{\partial \bar{\theta}} &= \frac{\partial}{\partial \theta'} \\ \frac{\partial}{\partial \bar{z}} &= \frac{\partial}{\partial z'} + \frac{\pi}{H} \frac{\partial}{\partial \theta'} \end{aligned} \quad (2.4)$$

Furthermore, for hydrodynamically fully developed flow conditions, the velocity profile is independent of z' coordinate, and

$$\frac{\partial \bar{u}}{\partial z'} = 0, \quad \frac{\partial \bar{v}}{\partial z'} = 0, \quad \frac{\partial \bar{w}}{\partial z'} = 0 \quad (2.5)$$

For thermally fully developed flow, on the other hand, the “invariant” temperature profile is mathematically represented by

$$\frac{\partial}{\partial z'} \left(\frac{T_w - \bar{T}}{T_w - \bar{T}_m} \right) = 0 \quad (2.6)$$

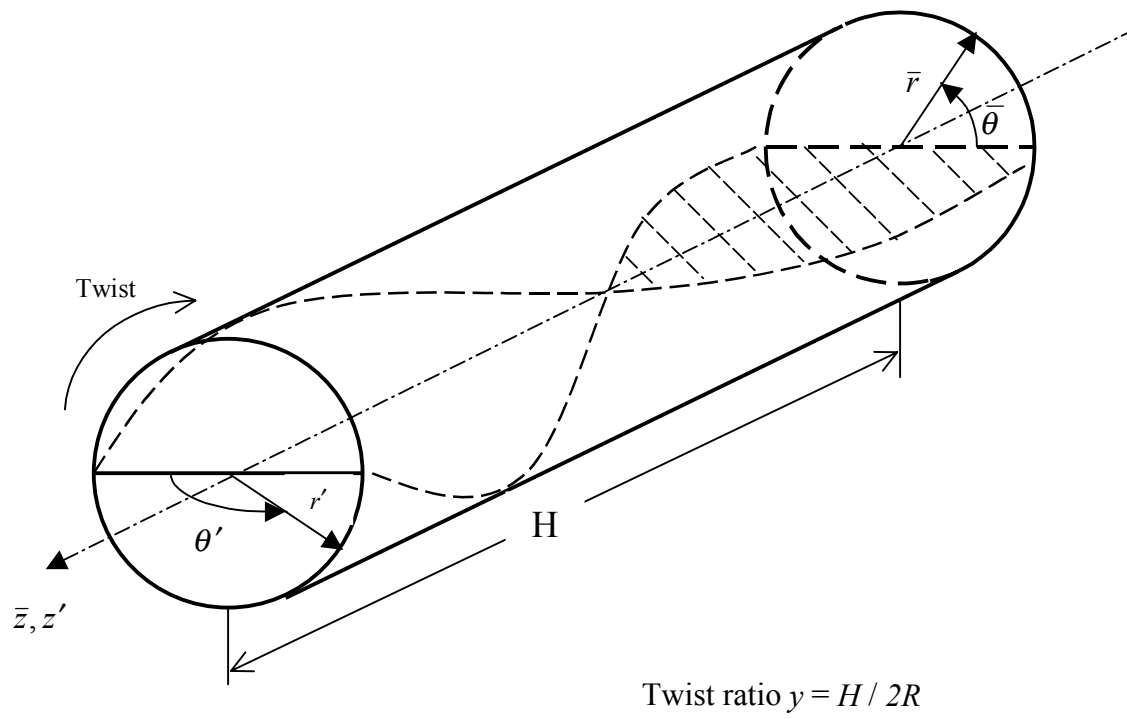


Fig. 2.3 Coordinate systems

The simplification of this equation yields

$$\frac{\partial \bar{T}}{\partial z'} = \left(\frac{T_w - \bar{T}}{T_w - \bar{T}_m} \right) \frac{d\bar{T}_m}{dz'} \quad (2.7a)$$

for the UWT boundary condition, and

$$\frac{\partial \bar{T}}{\partial z'} = \frac{dT_w}{dz'} = \frac{d\bar{T}_m}{dz'} \quad (2.7b)$$

for the UHF boundary condition. Thus, with these considerations, the governing equations of continuity, momentum, and energy can be stated in the helical coordinates as follows:

$$\frac{\partial \bar{u}}{\partial r'} + \frac{\bar{u}}{r'} + \frac{1}{r'} \frac{\partial \bar{v}}{\partial \theta'} + \frac{\pi}{H} \frac{\partial \bar{w}}{\partial \theta'} = 0 \quad (2.8a)$$

$$\begin{aligned} \bar{u} \frac{\partial \bar{w}}{\partial r'} + \frac{\bar{v}}{r'} \frac{\partial \bar{w}}{\partial \theta'} + \frac{\pi \bar{w}}{H} \frac{\partial \bar{w}}{\partial \theta'} = -\frac{1}{\rho} \frac{\partial \bar{p}}{\partial z'} \\ + \nu \left[\frac{1}{r'} \frac{\partial}{\partial r'} \left(r' \frac{\partial \bar{w}}{\partial r'} \right) + \left(\frac{1}{r'^2} + \frac{\pi^2}{H^2} \right) \frac{\partial^2 \bar{w}}{\partial \theta'^2} \right] \end{aligned} \quad (2.8b)$$

$$\begin{aligned} \bar{u} \frac{\partial \bar{u}}{\partial r'} + \frac{\bar{v}}{r'} \frac{\partial \bar{u}}{\partial \theta'} - \frac{\bar{v}^2}{r'} + \frac{\pi \bar{w}}{H} \frac{\partial \bar{u}}{\partial \theta'} = -\frac{1}{\rho} \frac{\partial \bar{p}}{\partial r'} \\ + \nu \left[\frac{1}{r'} \frac{\partial}{\partial r'} \left(r' \frac{\partial \bar{u}}{\partial r'} \right) - \frac{\bar{u}}{r'^2} + \left(\frac{1}{r'^2} + \frac{\pi^2}{H^2} \right) \frac{\partial^2 \bar{u}}{\partial \theta'^2} - \frac{2}{r'^2} \frac{\partial \bar{v}}{\partial \theta'} \right] \end{aligned} \quad (2.8c)$$

$$\begin{aligned} \bar{u} \frac{\partial \bar{v}}{\partial r'} + \frac{\bar{v}}{r'} \frac{\partial \bar{v}}{\partial \theta'} - \frac{\bar{u} \bar{v}}{r'} + \frac{\pi \bar{w}}{H} \frac{\partial \bar{v}}{\partial \theta'} = -\frac{1}{\rho} \frac{\partial \bar{p}}{\partial \theta'} \\ + \nu \left[\frac{1}{r'} \frac{\partial}{\partial r'} \left(r' \frac{\partial \bar{v}}{\partial r'} \right) - \frac{\bar{v}}{r'^2} + \left(\frac{1}{r'^2} + \frac{\pi^2}{H^2} \right) \frac{\partial^2 \bar{v}}{\partial \theta'^2} + \frac{2}{r'^2} \frac{\partial \bar{u}}{\partial \theta'} \right] \end{aligned} \quad (2.8d)$$

$$\begin{aligned} \bar{u} \frac{\partial \bar{T}}{\partial r'} + \frac{\bar{v}}{r'} \frac{\partial \bar{T}}{\partial \theta'} + \bar{w} \frac{\partial \bar{T}}{\partial z} + \frac{\pi \bar{w}}{H} \frac{\partial \bar{T}}{\partial \theta'} = \\ \alpha \left[\frac{1}{r'} \frac{\partial}{\partial r'} \left(r' \frac{\partial \bar{T}}{\partial r'} \right) + \left(\frac{1}{r'^2} + \frac{\pi^2}{H^2} \right) \frac{\partial^2 \bar{T}}{\partial \theta'^2} \right] \end{aligned} \quad (2.8e)$$

These are essentially two-dimensional equations, because $(d\bar{p}/dz')$ is a known constant, and the dependent variables $\bar{u}, \bar{v}, \bar{w}$ and \bar{T} are functions of r' and θ' only. Equations (2.8a) – (2.8d) are subject to the no-slip wall boundary condition, i.e.,

$$\bar{u} = \bar{v} = \bar{w} = 0 \quad (2.9)$$

at both the tube wall and the tape surface. For the temperature problem of Equation (2.8e), as explained in the previous sub-section, the two different wall boundary conditions considered here are as follows

$$\text{Case 1: } \quad \bar{T} = T_w \text{ at both the tube wall and the tape surface} \quad (2.10a)$$

$$\text{Case 2: } \quad \bar{T} = T_w \text{ at the tube wall, and}$$

$$\frac{\partial \bar{T}}{\partial n} = 0 \text{ at the tape surface.} \quad (2.10b)$$

Equation (2.10) holds good for both UWT and UHF conditions.

2.2.2 Stream function and vorticity formulation

From the point of view of numerical solutions, the presence of pressure p in the momentum equations poses certain computational difficulties. It may be noted that while cross-differentiating the radial and tangential momentum equations can eliminate the pressure terms, it renders the equations to have third-order terms. However, this can be remedied by introducing vorticity $\bar{\zeta}$, which is defined as the axial component of the curl of the velocity vector as follows:

$$\bar{\zeta} = \nabla \times \bar{V} \Big|_{z'} = \frac{1}{r'} \left[\frac{\partial}{\partial r'} (r' \bar{v}) - \frac{\partial \bar{u}}{\partial \theta'} \right] \quad (2.11)$$

The vorticity equation can then be developed by differentiating Eq. (2.8c) with respect to θ' , and Eq. (2.8d) with respect to r' , and subtracting the first from the second. Thus, by using the definition in Eq. (2.11), the resulting expression for the vorticity equation is

$$\begin{aligned} v \left[\frac{1}{r'} \frac{\partial}{\partial r'} \left(r' \frac{\partial \bar{\zeta}}{\partial r'} \right) + \left(\frac{1}{r'^2} + \frac{\pi^2}{H^2} \right) \frac{\partial^2 \bar{\zeta}}{\partial \theta'^2} \right] - \frac{1}{r'} \left[\frac{\partial \bar{\psi}}{\partial \theta'} \frac{\partial \bar{\zeta}}{\partial r'} - \frac{\partial \bar{\psi}}{\partial r'} \frac{\partial \bar{\zeta}}{\partial \theta'} \right] = \\ \frac{\pi}{H} \left\{ \frac{\partial \bar{w}}{\partial \theta'} \left[\frac{\partial^2 \bar{\psi}}{\partial r'^2} + \frac{1}{r'} \frac{\partial \bar{\psi}}{\partial r'} + \frac{2\pi}{H} \bar{w} \right] - \frac{\partial \bar{w}}{\partial r'} \frac{\partial^2 \bar{\psi}}{\partial r' \theta'} \right\} \end{aligned} \quad (2.12)$$

Next, the stream function $\bar{\psi}$ can be introduced such that the mass conservation is implicitly satisfied, and $\bar{\psi}$ is defined as:

$$\begin{aligned} \frac{\partial \bar{\psi}}{\partial \theta'} &= r' \bar{u} \\ \frac{\partial \bar{\psi}}{\partial r'} &= - \left(\bar{v} + \frac{\pi r'}{H} \bar{w} \right) \end{aligned} \quad (2.13)$$

This along with the definition of vorticity yields the following stream function equation:

$$\frac{1}{r'} \frac{\partial}{\partial r'} \left(r' \frac{\partial \bar{\psi}}{\partial r'} \right) + \frac{1}{r'^2} \frac{\partial^2 \bar{\psi}}{\partial \theta'^2} + \frac{\pi}{H r'} \frac{\partial}{\partial r'} (r'^2 \bar{w}) + \bar{\zeta} = 0 \quad (2.14)$$

The essential advantages of considering the $\bar{\psi}$ and $\bar{\zeta}$ formulation of the problem can be summed up as follows:

- Because the stream function equation satisfies mass conservation exactly, no explicit resource to the continuity equation is necessary.
- With the introduction of $\bar{\zeta}$, the radial and tangential momentum equations are replaced by a single equation for $\bar{\zeta}$.

Thus, the equations for stream function $\bar{\psi}$, vorticity $\bar{\zeta}$, axial velocity \bar{w} and temperature \bar{T} , Eqs. (2.14), (2.12), (2.8b), and (2.8e), respectively, provide the complete mathematical description of the twisted-tape-induced swirl flow and heat transfer problem. The no-slip

condition for velocity implies that the stream function has a constant value at the boundaries; this is set to zero for convenience here. The boundary conditions for vorticity, on the other hand, can be derived from its own definition, and can be mathematically stated as follows

(i) $r' = R, 0 < \theta < \pi$:

$$\bar{\zeta} = -\left(\frac{\partial^2 \bar{\psi}}{\partial r'^2} + \frac{\pi}{2y} \frac{\partial \bar{w}}{\partial r'}\right) \quad (2.15a)$$

(ii) $0 < r' \leq 1, \theta = 0 \text{ or } \pi$:

$$\bar{\zeta} = -\frac{1}{r'^2} \frac{\partial^2 \bar{\psi}}{\partial \theta'^2} \quad (2.15b)$$

(iii) $r' = 0, 0 \leq \theta \leq \pi$:

$$\bar{\zeta} = -2 \frac{\partial^2 \bar{\psi}}{\partial r'^2} \quad (2.15c)$$

2.2.3 Dimensionless formulation

The transformed governing differential equations can be restated in a dimensionless form by introducing the following variables:

$$r = \frac{r'}{R}, \quad \theta = \theta', \quad z = \frac{z'}{R}, \quad y = \frac{H}{2R} \quad (2.16)$$

$$\psi = \frac{\bar{\psi}}{v}, \quad \zeta = \frac{\bar{\zeta}}{v/R^2}, \quad w = \frac{\bar{w}}{v/R} \quad (2.17a)$$

$$G = \frac{-(\bar{p}/d\bar{z})}{\rho v^2 / R^3}, \quad T = \frac{\alpha(T_w - \bar{T})}{R^2 \bar{w}_m (d\bar{T}_m / d\bar{z})} \quad (2.17b)$$

Thus, the governing equations can be re-written as

Stream function equation:

$$\frac{1}{r} \frac{\partial}{\partial r} \left(r \frac{\partial \psi}{\partial r} \right) + \frac{1}{r^2} \frac{\partial^2 \psi}{\partial \theta^2} + \frac{\pi}{2yr} \frac{\partial}{\partial r} (r^2 w) + \zeta = 0 \quad (2.18a)$$

Vorticity equation:

$$\begin{aligned} & \left[\frac{1}{r} \frac{\partial}{\partial r} \left(r \frac{\partial \zeta}{\partial r} \right) + \left(\frac{1}{r^2} + \frac{\pi^2}{4y^2} \right) \frac{\partial^2 \zeta}{\partial \theta^2} \right] - \frac{1}{r} \left[\frac{\partial \psi}{\partial \theta} \frac{\partial \zeta}{\partial r} - \frac{\partial \psi}{\partial r} \frac{\partial \zeta}{\partial \theta} \right] = \\ & \frac{\pi}{2y} \left\{ \frac{\partial w}{\partial \theta} \left[\frac{\partial^2 \psi}{\partial r^2} + \frac{1}{r} \frac{\partial \psi}{\partial r} + \frac{\pi}{y} w \right] - \frac{\partial w}{\partial r} \frac{\partial^2 \psi}{\partial r \theta} \right\} \end{aligned} \quad (2.18b)$$

Axial velocity equation:

$$\left[\frac{1}{r} \frac{\partial}{\partial r} \left(r \frac{\partial w}{\partial r} \right) + \left(\frac{1}{r^2} + \frac{\pi^2}{4y^2} \right) \frac{\partial^2 w}{\partial \theta^2} \right] - \frac{1}{r} \left[\frac{\partial \psi}{\partial \theta} \frac{\partial w}{\partial r} - \frac{\partial \psi}{\partial r} \frac{\partial w}{\partial \theta} \right] + G = 0 \quad (2.18c)$$

Energy Equation for the UWT condition:

$$\left[\frac{1}{r} \frac{\partial}{\partial r} \left(r \frac{\partial T}{\partial r} \right) + \left(\frac{1}{r^2} + \frac{\pi^2}{4y^2} \right) \frac{\partial^2 T}{\partial \theta^2} \right] - \frac{\text{Pr}}{r} \left[\frac{\partial \psi}{\partial \theta} \frac{\partial T}{\partial r} - \frac{\partial \psi}{\partial r} \frac{\partial T}{\partial \theta} \right] + \frac{wT}{w_m T_m} = 0 \quad (2.18d)$$

Energy equation for the UHF condition:

$$\left[\frac{1}{r} \frac{\partial}{\partial r} \left(r \frac{\partial T}{\partial r} \right) + \left(\frac{1}{r^2} + \frac{\pi^2}{4y^2} \right) \frac{\partial^2 T}{\partial \theta^2} \right] - \frac{\text{Pr}}{r} \left[\frac{\partial \psi}{\partial \theta} \frac{\partial T}{\partial r} - \frac{\partial \psi}{\partial r} \frac{\partial T}{\partial \theta} \right] + \frac{w}{w_m} = 0 \quad (2.18e)$$

A review of these equations shows that the dimensionless velocity profile is independent of fluid properties whereas the dimensionless temperature profile is influenced by the fluid Prandtl number.

2.2.4 Generalized presentation of governing equations

It should be noted that each of the governing differential equations that need to be solved contain similar terms. With each dependent variable represented by a general function ϕ , the following common terms can be identified:

Convective terms:

$$\frac{1}{r} \left(\frac{\partial \psi}{\partial \theta} \frac{\partial \phi}{\partial r} - \frac{\partial \psi}{\partial r} \frac{\partial \phi}{\partial \theta} \right)$$

Diffusive terms:

$$\frac{1}{r} \frac{\partial}{\partial r} \left(r \frac{\partial \phi}{\partial r} \right) + \left[\frac{1}{r^2} + \left(\frac{\pi}{2y} \right)^2 \right] \frac{\partial^2 \phi}{\partial \theta^2}$$

The only exception is in the stream function equation where the coefficients for its convective terms are zero. The remaining parts of the differential equations can be included in one single term - source term. Thus a general equation for all dependent variables can be written as

$$\frac{1}{r} \frac{\partial}{\partial r} \left(r \frac{\partial \phi}{\partial r} \right) - \frac{1}{r} \lambda \frac{\partial \phi}{\partial r} + \frac{1}{r} \beta \frac{\partial^2 \phi}{\partial r^2} - \frac{1}{r} \mu \frac{\partial \phi}{\partial \theta} + S_\phi = 0 \quad (2.19)$$

where expressions for λ , β , μ , and S_ϕ for each dependent variable representation in ϕ is given in Table 2.1. Also, the boundary conditions for each case are summarized in Table 2.2.

2.3 Friction Factor and Nusselt Number

Knowing the velocity and temperature distributions, the global parameters of engineering interest, the isothermal friction factor and the Nusselt Number, and their variation with flow Reynolds number and tape-insert ratio can be calculated. These are essentially based on the average wall shear stress and wall heat flux, respectively.

The Fanning friction factor is generally defined as

$$f = \frac{\tau_w}{\frac{1}{2} \rho \bar{w}_m^2} \quad (2.20)$$

Table 2.1 General Equations for ψ , ζ , w and T

ϕ	λ	β	μ	S_ϕ
ψ	0	$\frac{1}{r}$	0	$\frac{\pi r}{2y} \cdot \frac{\partial w}{\partial r} + \frac{\pi w}{y} + \zeta$
ζ	$\frac{\partial \psi}{\partial \theta}$	$\frac{1}{r} + r \left(\frac{\pi}{2y} \right)^2$	$-\frac{\partial \psi}{\partial r}$	S_ζ^*
w	$\frac{\partial \psi}{\partial \theta}$	$\frac{1}{r} + r \left(\frac{\pi}{2y} \right)^2$	$-\frac{\partial \psi}{\partial r}$	G
T	$\text{Pr} \frac{\partial \psi}{\partial \theta}$	$\frac{1}{r} + r \left(\frac{\pi}{2y} \right)^2$	$-\text{Pr} \frac{\partial \psi}{\partial r}$	$\frac{w}{w_m} \cdot \frac{T}{T_m}$ for UWT $\frac{w}{w_m}$ for UHF

* The term S_ζ is as follows:

$$S_\zeta = -\frac{\pi}{2y} \left[\frac{\partial w}{\partial \theta} \left(\frac{\partial^2 \psi}{\partial r^2} + \frac{1}{r} \frac{\partial \psi}{\partial r} + \frac{\pi}{y} w \right) - \frac{\partial w}{\partial r} \frac{\partial^2 \psi}{\partial r \partial \theta} \right]$$

Table 2.2 Boundary conditions for ψ , ζ , w and T

ϕ	$0 < r \leq 1, \theta = 0$	$r = 1, 0 \leq \theta \leq \pi$	$0 < r \leq 1, \theta = \pi$	$r = 0, 0 \leq \theta \leq \pi$
ψ	0	0	0	0
ζ	$-\frac{1}{r^2} \frac{\partial^2 \psi}{\partial \theta^2}$	$-\left(\frac{\partial^2 \psi}{\partial r^2} + \frac{\pi}{2y} \frac{\partial w}{\partial r} \right)$	$-\frac{1}{r^2} \frac{\partial^2 \psi}{\partial \theta^2}$	$-\frac{\partial^2 \psi}{\partial r^2}$
w	0	0	0	0
T (Case 1)	0	0	0	0
(Case 2)	$\frac{\partial T}{\partial \theta} = 0$	0	$\frac{\partial T}{\partial \theta} = 0$	$\frac{\partial T}{\partial r} = 0$

where the axial mean velocity is given by its usual definition

$$\bar{w}_m = \frac{2}{\pi R^2} \int_0^R \int_0^\pi \bar{w} r' d\theta' dr' \quad (2.21)$$

The average wall shear stress can be obtained from a force balance in terms of the constant pressure gradient as

$$\tau_w = \frac{R}{2} \left(\frac{\pi}{\pi + 2} \right) \left(\frac{d\bar{p}}{dz} \right) \quad (2.22)$$

Thus, in terms of dimensionless variables, the friction factor can be expressed as

$$f = \frac{G}{w_m^2} \left(\frac{\pi}{\pi + 2} \right) \text{ or } f \text{ Re} = \frac{4G}{\text{Re}} \left(\frac{\pi}{\pi + 2} \right) \quad (2.23)$$

It should be noted that Eq. (2.23) is based on the hydraulic diameter d_h , which is given by

$$d_h = \frac{\pi}{\pi + 2} d \quad (2.24)$$

However, as per the recommendation of Marner et al. (1983), it is preferable to present enhancement results in terms of the tube inner diameter. In this case, Eq. (2.24) reduce to

$$f \text{ Re} = \frac{4G}{\text{Re}} \quad (2.25)$$

The details of the development of these equations can be found in Appendix A.

Similarly, from the fully-developed swirl flow temperature distribution and its variation with Re, Pr, and y , the Nusselt number can be determined from its usual definition. This can be restated, as shown in Appendix B, in terms of the axial enthalpy change of the fluid for the two cases of the thermal boundary condition as follows:

$$Nu = \begin{cases} \frac{1}{T_m} \frac{\pi}{\pi + 2}, & \text{for Case 1} \\ \frac{1}{T_m}, & \text{for Case 2} \end{cases} \quad (2.26)$$

Here the dimensionless bulk-mean fluid temperature is given by

$$T_m = \frac{2}{\pi w_m} \int_0^1 \int_0^\pi w T r d\theta dr \quad (2.27)$$

Another way to calculate the Nusselt number is to integrate the local-wall temperature gradients over the heated perimeters of the duct. This approach produces the following different expressions for the average Nusselt number:

$$Nu = \begin{cases} \frac{\pi}{(\pi + 2)T_m} \left(\int_0^\pi \frac{\partial T}{\partial r} d\theta + \int_{-1}^1 \frac{\partial T}{r \partial \theta} dr \right) & \text{for Case 1} \\ \frac{2}{\pi T_m} \int_0^\pi \frac{\partial T}{\partial r} d\theta, & \text{for Case 2} \end{cases} \quad (2.28)$$

Note that both Eqs. (2.26) and (2.28) are based on the tube inside diameter in accordance with the Marner et al. (1983) recommendations. The detailed formulation for these expressions is outlined in Appendix B.

CHAPTER 3. NUMERICAL SOLUTION

Techniques for obtaining numerical solutions of elliptic partial differential equations that govern two-dimensional flows and their applications have long been reported in literature. One of the earliest works was perhaps that of Thom (1933), who considered the flow around a circular cylinder. The resulting algebraic equations were solved by an iterative, successive substitution procedure; a solution instability problem occurred, however, at high Reynolds number flows. In much of the computational literature, several different strategies have evolved to address this difficulty as well as some others that are typically encountered in two-dimensional problems and their associated non-linear flow equations (Anderson et al., 1984; Jaluria, 1980; Patankar, 1975).

The accuracy and efficiency of numerical solutions, in general, depend on the method that is used to obtain the discretized equations and the subsequent convergence of the solution of the resulting non-linear algebraic equations. The main differences between these methods are associated with the manner in which the dependent variables for convection are approximated, and the discretization of the governing differential equations. A brief description of the three techniques that are most often used is given in the following.

Finite difference methods describe the unknowns ϕ of the flow problem by means of point samples at the node points of a grid of coordinate lines. Truncated Taylor series expansions are

often used to generate finite difference approximations for the derivatives of ϕ in terms of point samples of ϕ at each grid point and its immediate neighbors. These derivatives appearing in the governing equations are then replaced by finite difference representations, yielding an algebraic equation for the values of ϕ at each grid point. Smith (1985), Patankar (1975), and Anderson et al. (1984), among others, have given a comprehensive account of all aspects of the finite difference methods.

Finite element methods use simple piecewise functions (e.g. linear or quadratic) to describe the local variations of unknown flow variables ϕ and its conservation across a discrete element. If the piecewise approximating functions for ϕ are substituted into the governing differential equation, it will not hold exactly and a residual is defined to measure the errors. Next the residuals (and hence the errors) are minimized in some sense by multiplying them by a set of weighting functions and integration. As a result of this process, a set of algebraic equations is obtained for the unknown coefficients of the approximating functions, which are then solved iteratively. The theory of finite elements has been developed initially for structural stress analysis. A description of the techniques for fluid flow applications is given by Zienkiewicz and Taylor (1991).

Spectral Methods approximate the unknowns by means of truncated Fourier series or series of Chebyshev polynomials. Unlike the finite difference or finite element approaches, the approximations are not local but valid throughout the entire computational domain. Again the unknowns in the governing differential equations are replaced by the truncated series. To obtain the set of algebraic equations for the coefficients of the Fourier or Chebyshev series, the appropriate constraint is provided by a weighted residuals concept. This is similar to that used in the finite element method, where the approximate function is made to coincide with the exact

solution at a number of grid points. Extended aspects of this specialized method and its application can be found in Gottlieb and Orszag (1977).

3.1 Finite Control Volume Method

The finite volume method was originally developed as a special, "conservation" form of the finite difference formulation. The computational algorithm for obtaining a complete numerical solution consists of the following steps:

- Formal integration of the governing equations for fluid flow and heat energy transport over all the finite control volumes of the computational domain.
- Discretization by means of the substitution of a variety of finite-difference-type approximations for the terms in the integrated equation representing flow processes such as convection, diffusion, and sources. This converts the integral equations into a system of algebraic equations.
- Solution of the algebraic equations by an iterative method.

The first step, the control-volume integration, distinguishes the finite volume method from all other CFD techniques. The resulting statements express the exact conservation of relevant dependent properties (velocity and temperature, for example) for each finite-size cell. This clear relationship between the numerical algorithm and the underlying physical conservation principle forms one of the main attractions of the finite volume method, and makes its concepts much more simple to understand and apply to convective transport, in particular, than finite element and spectral methods. The conservation of a general flow variable ϕ , for example the velocity component or enthalpy, within a finite control volume can be generally expressed as a balance between the various fluxes as follows:

$$\left[\begin{array}{c} \text{Rate of change} \\ \text{of } \phi \text{ in the} \\ \text{control volume} \\ \text{with respect} \\ \text{to time} \end{array} \right] = \left[\begin{array}{c} \text{Net flux of} \\ \phi \text{ due to} \\ \text{convection} \\ \text{into the} \\ \text{control volume} \end{array} \right] + \left[\begin{array}{c} \text{Net flux of} \\ \phi \text{ due to} \\ \text{diffusion} \\ \text{into the} \\ \text{control volume} \end{array} \right] + \left[\begin{array}{c} \text{Net rate} \\ \text{of creation} \\ \text{of } \phi \\ \text{inside the} \\ \text{control volume} \end{array} \right]$$

This, when expressed as a differential equation, essentially forms the basis for the conservative form of the governing transport equations.

3.2 Discretization of Governing Differential Equation

The general differential equation that governs the transport of mass, momentum, and energy has been given in Chapter 2 (Section 2.2.3) as follows:

$$\frac{1}{r} \frac{\partial}{\partial r} \left(r \frac{\partial \phi}{\partial r} \right) - \frac{1}{r} \lambda \frac{\partial \phi}{\partial r} + \frac{1}{r} \beta \frac{\partial^2 \phi}{\partial r^2} - \frac{1}{r} \mu \frac{\partial \phi}{\partial \theta} + S_\phi = 0 \quad (2.19)$$

The corresponding boundary conditions for each dependent variable are listed in Table 2.2. The finite control-volume procedure adopted to solve this type of partial differential equation is described in detail by Patankar (1980), and a detailed example of applying the central-differencing scheme is outlined in Appendix C. Therefore, only the final discretization equations are presented here.

The partial differential equation (2.19) is basically converted into a set of algebraic equations that can be expressed as

$$a_P \phi_P = a_W \phi_W + a_E \phi_E + a_N \phi_N + a_S \phi_S + b \quad (3.1)$$

where a 's are the coefficients that determine the relative "weighting" of the neighboring values of ϕ in the evaluation of ϕ_P . The effects of sources of ϕ are contained in the term b . There is one such equation for each variable ϕ at every interior node of the grid (node referred to by P in

Fig. C.1), with conditions specified on boundary nodes. Therefore, there will be as many equations as there are unknowns. The set of algebraic equations given by Eq. (3.1) can be solved by an iterative procedure. The iterative calculations are required because the a 's and b depend upon the values of ϕ 's and the strength of convective and diffusive fluxes, as shown below.

$$\begin{aligned}
a_W &= D_w A(|P_w|) + \max\{-F_w, 0\} \\
a_E &= D_e A(|P_e|) + \max\{F_e, 0\} \\
a_N &= D_n A(|P_n|) + \max\{-F_n, 0\} \\
a_S &= D_s A(|P_s|) + \max\{F_s, 0\} \\
a_P &= a_W + a_E + a_N + a_S \\
b &= S_\phi \cdot r \cdot \Delta r \cdot \Delta\theta
\end{aligned} \tag{3.2}$$

where F 's represent the following convective fluxes:

$$\begin{aligned}
F_n &= \lambda_n \cdot \Delta\theta, & F_s &= \lambda_s \cdot \Delta\theta \\
F_w &= \mu_w \cdot \Delta r, & F_e &= \mu_e \cdot \Delta r
\end{aligned} \tag{3.3}$$

and D 's represent the following diffusive fluxes:

$$\begin{aligned}
D_n &= r_n \cdot \Delta\theta / \Delta r, & D_s &= r_s \cdot \Delta\theta / \Delta r \\
D_w &= \beta_w \cdot \Delta r / \Delta\theta, & D_e &= \beta_e \cdot \Delta r / \Delta\theta
\end{aligned} \tag{3.4}$$

and $A(|P|)$ is a function of Peclet number ($P = F / D$), which has different forms for various schemes, such as upwind and power-law, etc. (see Appendix C for details).

It should be noted from the derivation of Eq. (3.1) that only the diffusive terms and the source term are always discretized by central difference approximation, whereas the convective terms are treated by various schemes (upwind, power-law, etc.).

3.3 Solution Procedure

The Gauss-Seidel iteration procedure is adopted to solve the set of algebraic equations given by Eq. (3.1), incorporating the line-by-line successive substitution (or relaxation) formula. For the twisted-tape flow equations described in Chapter 2, this standard iteration procedure does not always produce convergence. For instance, in computations at high Re and low y , the source term of vorticity equation becomes very large. Under these conditions, a given flow perturbation (i.e. a change in w and ψ) produces a large change in ζ_p . This change in ζ_p causes the stream function to be altered greatly, because ζ_p appears in the source term of the stream function equation. This greatly altered stream function distribution in turns perturbs the flow further. Clearly this computation scheme can become unstable, although the physical flow situation is a stable one. Gosman and Spalding (1970) suggested an iterative procedure to cure such an instability, which was called the “multi-point circulation adjustment” (MPCA) procedure. In the present study, the commonly used under-relaxation technique is employed to achieve convergence. It is found that this technique is simple and effective when only applied to the source term in the vorticity equation as follows:

$$S_{\zeta} = RF \cdot S_{\zeta}^{new} + (1 - RF) \cdot S_{\zeta}^{old} \quad (3.5)$$

The relaxation factor, RF , varied from 0.1 through 0.8, for Reynolds number up to 1200 and twist ratio y as low as 3.0.

As can be seen from Eqs. (2.18), the solution of the energy equation depends on the velocity distribution, but does not contribute to the hydraulic problem, i.e., they are decoupled. The solution strategy is then to first solve the equations of w, ψ and ζ to get convergent results, and subsequently use the predicted distribution of w and ψ , along with the input value of

Prandtl number, to solve for the temperature profile. The convergence criterion for the iterative solutions was imposed such that the relative error, defined as

$$\varepsilon = \left| \frac{\phi^{new} - \phi^{old}}{\phi^{old}} \right| \quad (3.6)$$

was than 10^{-6} . Here, the error in ϕ mainly represents the vorticity ζ , because it is usually the "last" variable to convergent. All the numerical integrations, required to obtain the mean axial velocity and bulk-mean fluid temperature, were performed using the Simpson scheme. Furthermore, wall-derivatives were calculated by a second-order differencing (Tannehill et al., 1997).

The procedure to solve the discretised equations of w , ψ and ζ includes the following steps:

- (1) Input Re and y : the twist ratio y is determined by the geometry and thus is a natural input. Some previous studies took the pressure drop $d\bar{p}/dz'$ as a known value and then calculated Reynolds number from the velocity profile. Here Re is given and the pressure drop constant G is evaluated during the computation. This treatment provides obvious one-on-one relations between Re, f , and Nu .
- (2) Initialize the distributions of w , ψ and ζ . For low Re and large y , they can be considered to be uniform over the cross section and set at zeros. It was found that much more iterations were required for high Re and small y . To obtain convergence quickly for these cases, the solutions for low Re and large y were used as "initial" profiles of w , ψ and ζ for subsequent cases with higher Re and/or smaller y .
- (3) Calculate the normalized axial velocity \hat{w} from its definition

$$\hat{w} = \frac{w}{G} \quad (3.7)$$

whereby the constant G in the axial momentum equation is eliminated and the source term reduces to unity. The iterative solution for \hat{w} , ψ and ζ is then obtained, in which every interior node is swept once and their values are updated instantaneously.

- (4) Evaluate the pressure drop constant G . Once the profile of \hat{w} is updated, the value of G is given by (see Appendix A for details)

$$G = \frac{\pi \text{Re}}{4 \int_0^1 \int_0^\pi \hat{w} r d\theta dr} \quad (3.8)$$

- (5) Convert \hat{w} into w via Eq. (3.7) for the computations of ψ and ζ .
- (6) Compute the stream function ψ . A linear algorithm was suggested by Yang (1986) for such highly nonlinear system of equations. Here ψ and ζ are still solved separately because convergence has been guaranteed.
- (7) Compute the vorticity ζ . This is incorporated with the under-relaxation of the source term. Before sweeping the interior nodes, the values of ζ at boundary nodes need to be specified using the updated distribution of w and ψ (see Appendix E for details).
- (8) Check the relative error ε . If $\varepsilon < 10^{-6}$, it can be concluded that convergence is achieved. Otherwise, Steps (3) through (7) need to be repeated.

The grid size or meshing of the computational domain is important for obtaining accurate solutions. Generally, the more cells the domain is divided into, the closer the results approach the exact solutions. The difference between various schemes also becomes smaller. This does not, however, justify that the grid can be established to be as small as possible, because the memory capacity of the computer and the running speed may pose a problem. An appropriate number of grid points should be such that the computational memory requirement is met with the hardware and the running time is acceptable, and yet "good" accuracy is ensured.

A numerical experiment was conducted on a 400 MHz personal computer to find out the optimum grid size: a particular case was selected at $Re = 400$, and $y = 3$, and the grid size varied from 11×21 to 31×91 (radical \times angular). The numerical results fRe , the relative improvement compared to previous larger grid size, and the computational time are listed in the following table. As can be seen, the numerical results are improved by increasing the number of grids; however, the difference becomes insignificant and the convergence time increases dramatically. The optimum grid size should be such that further mesh refinement would not have much effect on the numerical results and the time consumption is tremendous. Therefore, the grid size 21×61 is selected for the computational domain.

Table 3.1 Numerical experiment results of grid size sensitivity ($Re = 400, y = 3$)

Grid size ($r \times \theta$)	11 x 21	11 x 31	21 x 31	21 x 41	21 x 61	31 x 61	31 x 91
fRe	55.76	54.62	53.74	53.31	53.02	52.83	52.70
Improvement (%)		2.04	1.61	0.80	0.54	0.36	0.25
Time (seconds)	2	8	34	57	97	212	493

CHAPTER 4. RESULTS AND DISCUSSIONS

The problem of constant properties, fully developed laminar swirl flow in a circular tube with a negligible thickness twisted-tape insert has been analyzed. This is computationally modeled as a helically twisted semi-circular tube. For the heat transfer problem, both the UWT and UHF thermal boundary conditions are considered, with the flat wall idealized as at UWT/UHF, or adiabatic. This study models the tape insert as having 100% or zero fin efficiency. Fluid flow and heat transfer results are obtained for the following range of conditions:

$$y = 3, 6, 12, \infty$$

$$\text{Pr} = 1, 6, 80$$

$$20 \leq \text{Re} \leq 1200$$

The velocity and temperature distributions, and the associated friction factors and Nusselt numbers are presented in the ensuing sections.

4.1 Flow Field

The laminar flow field is strongly influenced by the flow Reynolds number and twist ratio y . To illustrate this, it is instructive to consider the cross-section velocity vectors along with the stream function ψ and axial velocity profiles. To make the cross-section velocity vector plots, the

radial velocity (u) and tangential velocity (v) can be calculated from the definition of stream function in two different ways. One is to consider

$$u = \frac{1}{r} \frac{\partial \psi}{\partial \theta}, \quad v = -\frac{\partial \psi}{\partial r} - \frac{\pi}{2y} r \omega \quad (4.1)$$

which is based on the dimensionless helical coordinates (r, θ, z) , and implies that we observe the flow field standing on the surface of the twisted tape moving axially with its twist. This is an incorrect representation, and the actual velocity vectors have to be based on the stationary cylindrical coordinates $(\bar{r}, \bar{\theta}, \bar{z})$, and u and v are given by

$$u = \frac{1}{r} \frac{\partial \psi}{\partial \theta}, \quad v = -\frac{\partial \psi}{\partial r} \quad (4.2)$$

Also, the graphing of the actual velocity vectors requires that the velocity components be on the Cartesian coordinates further transformed as follows

$$u_{xy} = u \cos \theta - v \sin \theta, \quad v_{xy} = u \sin \theta + v \cos \theta \quad (4.3)$$

The vectorial combination of u_{xy} and v_{xy} thus gives the cross-stream swirl flow field.

4.1.1 Velocity distribution

The centrifugal-type force that is induced by the helical curvature of the twisted-tape inserts is directly proportional to the square of Reynolds number and inversely proportional to twist ratio (Manglik and Bergles, 1993a; Manglik et al. 2001). Increasing Re or decreasing y essentially produces the same trends in the flow patterns. The influence of these two parameters on the velocity distribution, and their role in generating swirl flows are discussed in this section.

The stream function distribution, axial velocity contours, and cross-section velocity vector plot in Fig. 4.1 shows the effect of Re on the flow field with a fixed tape twist ratio $y = 3$. With

a clockwise rotation of the tape in the axial flow direction, the tape curvature-induced force is seen to produce an anti-clockwise secondary circulation in Fig. 4.1 (a). The consequent helical core-flow acceleration causes the mean axial peak velocity location to be skewed off-center in an anti-clockwise direction ($\bar{\theta} > 90$). As Re increases, a second re-circulation cell is formed near the $\bar{\theta} \approx 0$ flat tape surface. This vortex grows with Re to engulf almost half of the partitioned duct, and attains a strength comparable to that of the primary cell. This swirl behavior is also reflected in the axial velocity contour lines, which gradually tend to redistribute with increasing Re till a second peak of about equal size appears in the $\bar{\theta} < 90$ region. The influence of Re on the secondary flow structure is further illustrated in the cross-section velocity vectors in Fig. 4.1, where the onset and growth of a double-vortex swirl structure is clearly evident.

The influence of decreasing y , or increasing severity of tape twist, on the velocity distribution is illustrated in Fig. 4.2. Here the variations in ψ , w , and $\vec{V}_{r,\theta}$ with $y = 12, 6,$ and 3 , for a fixed flow rate of $Re = 800$ are graphed. The helical swirl flows that are generated by the curvature of the twisted tape are clearly seen. The single-cell vortex that develops with a gentler twist tape ($y = 12$), gradually grows into a two-cell structure, composed of two counter-rotating vortices of approximately equal size and magnitude, with increasing tape-twist severity ($y = 3$). Correspondingly, in the latter case, the axial velocity distribution shows two peaks near the core of the vortices. This swirl behavior with decreasing y ($12 \rightarrow 3$) with fixed $Re (= 800)$ is similar to that seen in Fig. 4.1 for fixed $y (= 3)$ and increasing $Re (= 200 \rightarrow 1000)$.

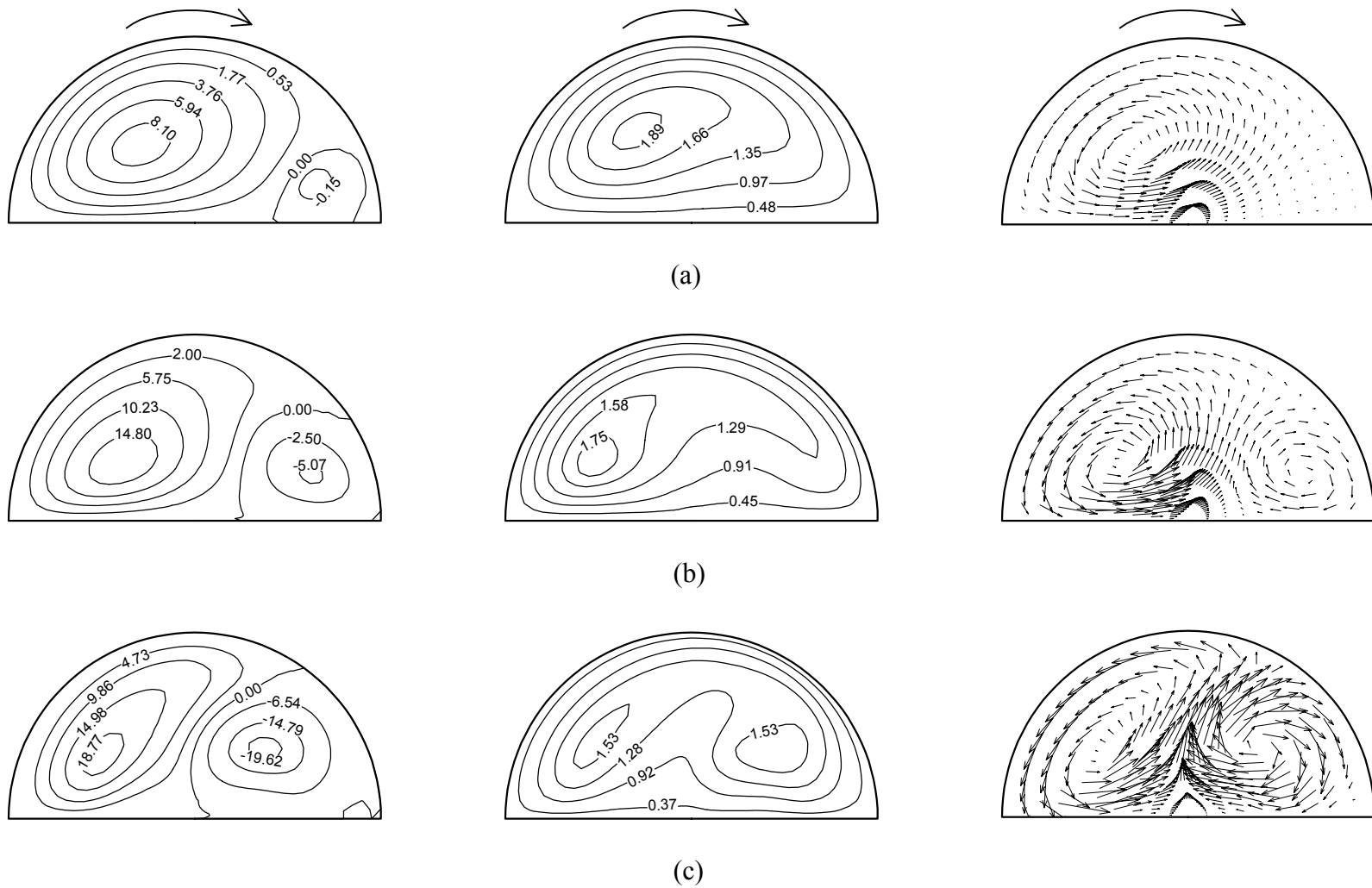


Fig. 4.1 Stream function, axial velocity and cross-section velocity vector distributions for $y = 3$, and (a) $Re = 200$, (b) $Re = 600$, and (c) $Re = 1000$.

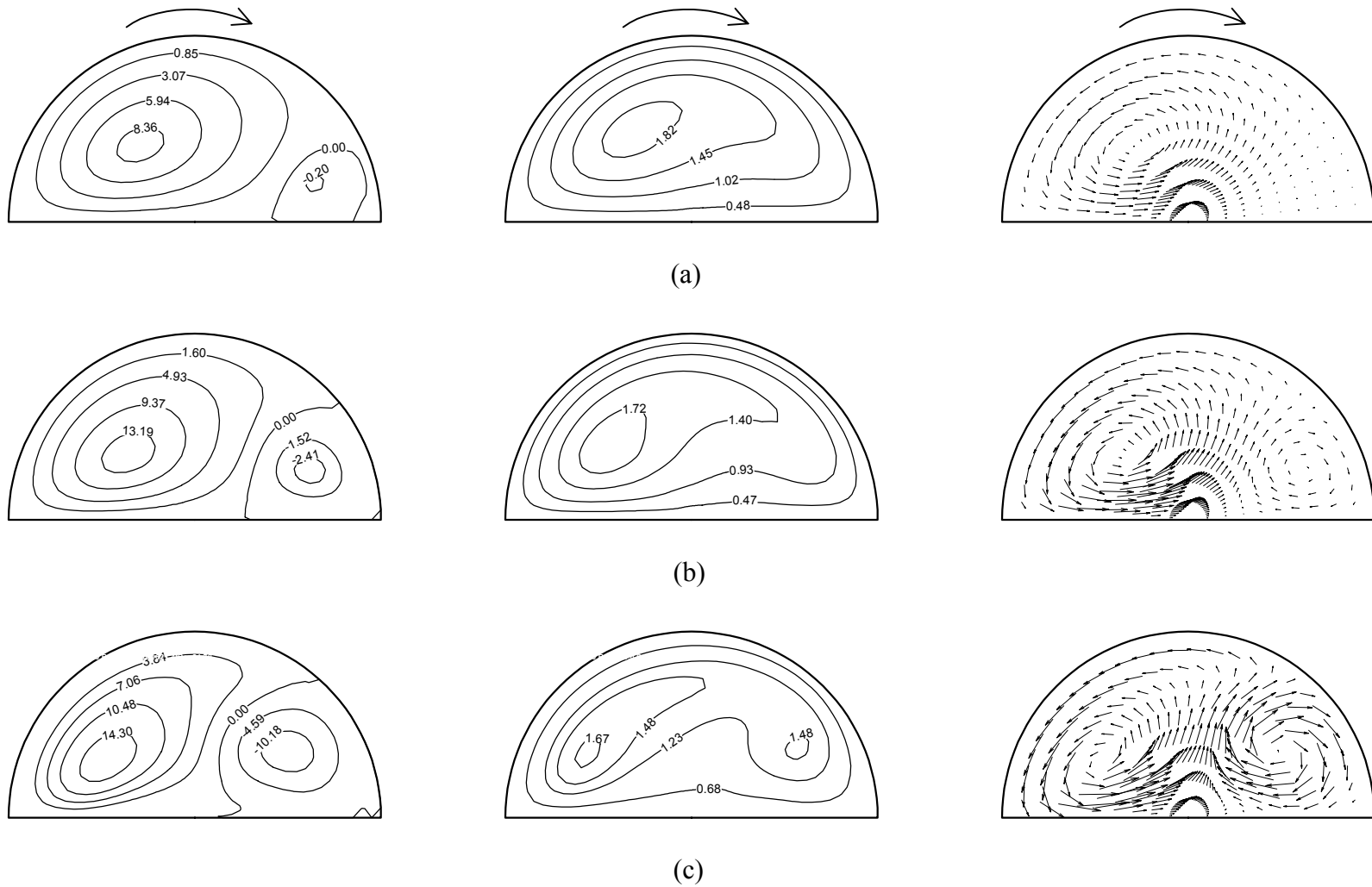


Fig. 4.2 Stream function, axial velocity and cross-section velocity vector distributions for $Re = 800$, and (a) $y = 12$, (b) $y = 6$, and (c) $y = 3$.

4.1.2 Shear stress distribution

The local shear stress distributions on the tube wall and surface of the twisted tape is useful in gaining an insight in the effects of tape-induced swirl on the axial flow resistance. The shear stress can be obtained from the local axial velocity distribution by its definition as

$$\bar{\tau} = -\mu \left. \frac{\partial \bar{w}}{\partial \bar{n}} \right|_{wall} \quad (4.4)$$

Here $(\partial \bar{w} / \partial \bar{n})_{wall}$ is the normal wall gradient of the axial velocity. Thus, in terms of the cylindrical coordinate system that describes the semi-circular flow cross-section geometry, the local wall shear stress can be stated as

$$\bar{\tau}_w = -\mu (\partial \bar{w} / \partial \bar{r}); \bar{r} = R, 0 < \bar{\theta} < \pi, \text{ and } \bar{r} = 0 \quad (4.5a)$$

$$\bar{\tau}_w = -(\mu / \bar{r}) (\partial \bar{w} / \partial \bar{\theta}); \bar{\theta} = 0 \text{ and } \pi, 0 < \bar{r} < R \quad (4.5b)$$

Equation (4.5) can again be recast in a dimensionless form by introducing

$$\tau = \bar{\tau} / (\rho v^2 / R^2) \quad (4.6)$$

and the dimensionless cylindrical coordinates and velocity of Eqs. (2.16) and (2.17a), respectively, to yield

$$\tau_w = -(\partial w / \partial r); r = 0 \text{ and } 1, 0 < \theta < \pi \quad (4.7a)$$

$$\tau_w = -(\partial w / \partial \theta); \theta = 0 \text{ and } \pi, 0 < r < 1 \quad (4.7b)$$

The influences of the tape-twist ratio y and flow Re on the wall shear stress distribution are shown in Figs. 4.3 and 4.4. The development of tape-induced swirl from a single-cell circulation into a double-cell structure is also seen in these figures. In Fig. 4.3, as y decreases ($12 \rightarrow 3$), the shear stress profile displays two peaks correspondingly to the two counter-rotating vortices that are formed with $y = 3$ and $Re = 800$. A similar

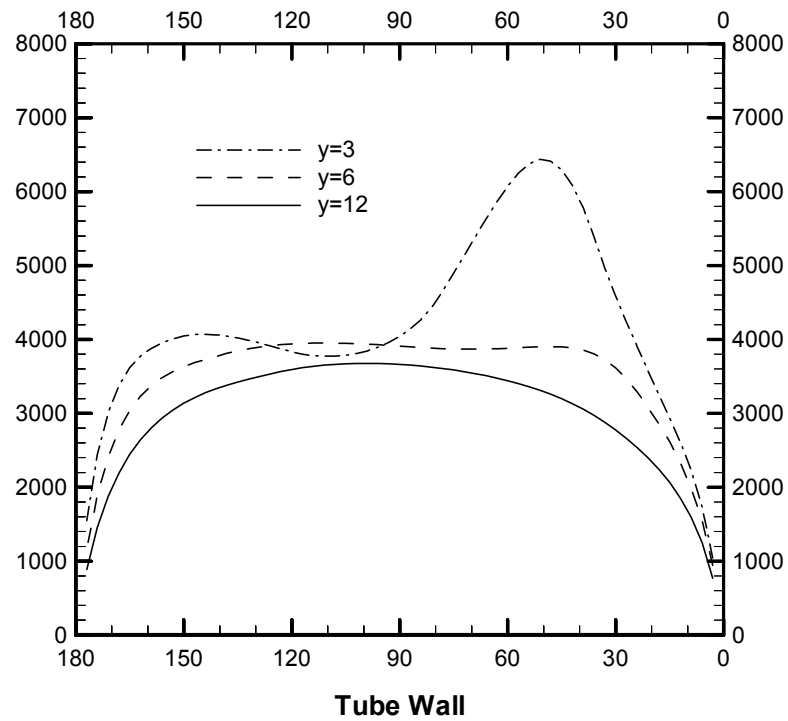
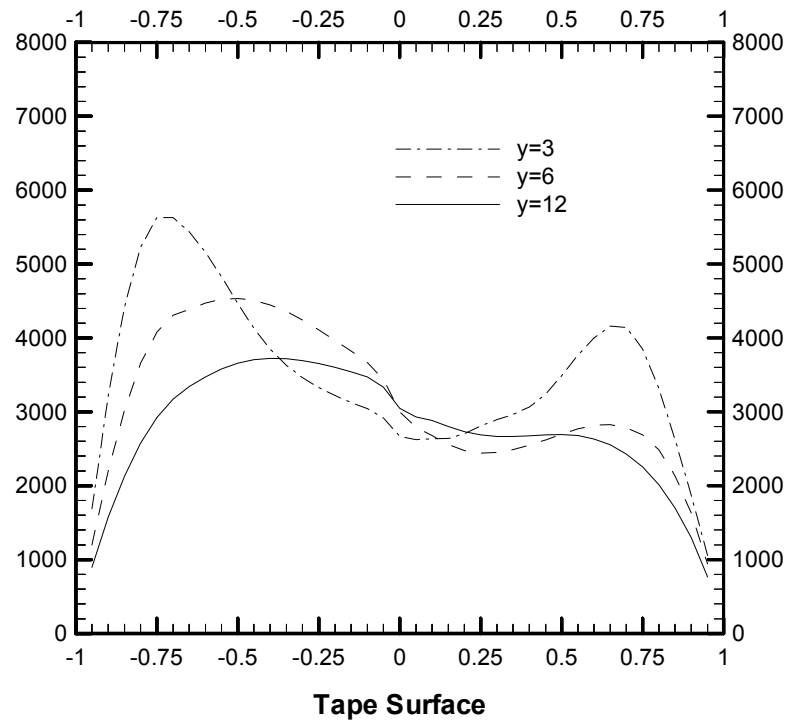


Fig. 4.3 Wall shear stress distribution for $Re = 800$ and $y = 3, 6,$ and 12

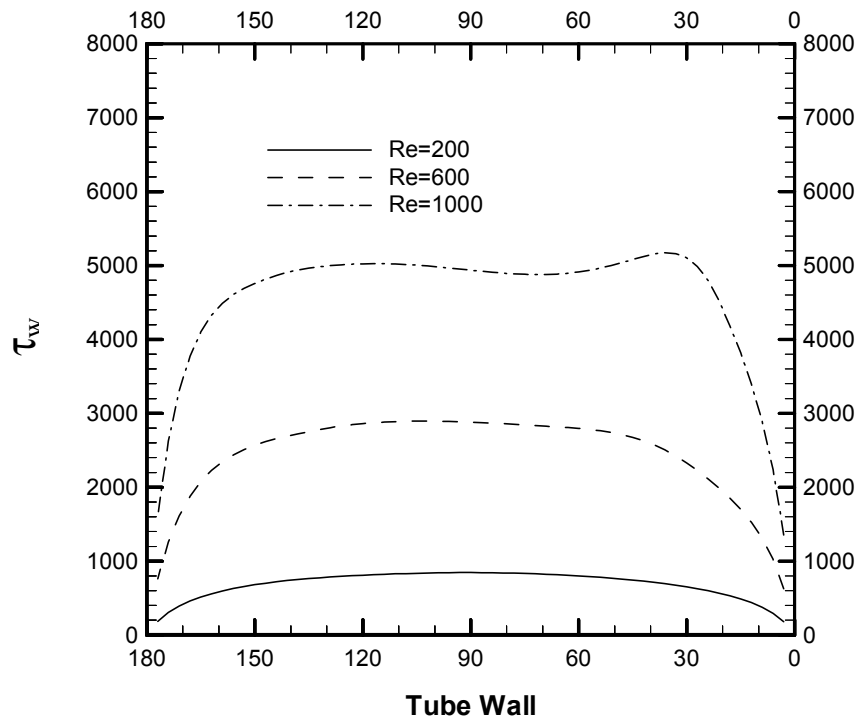
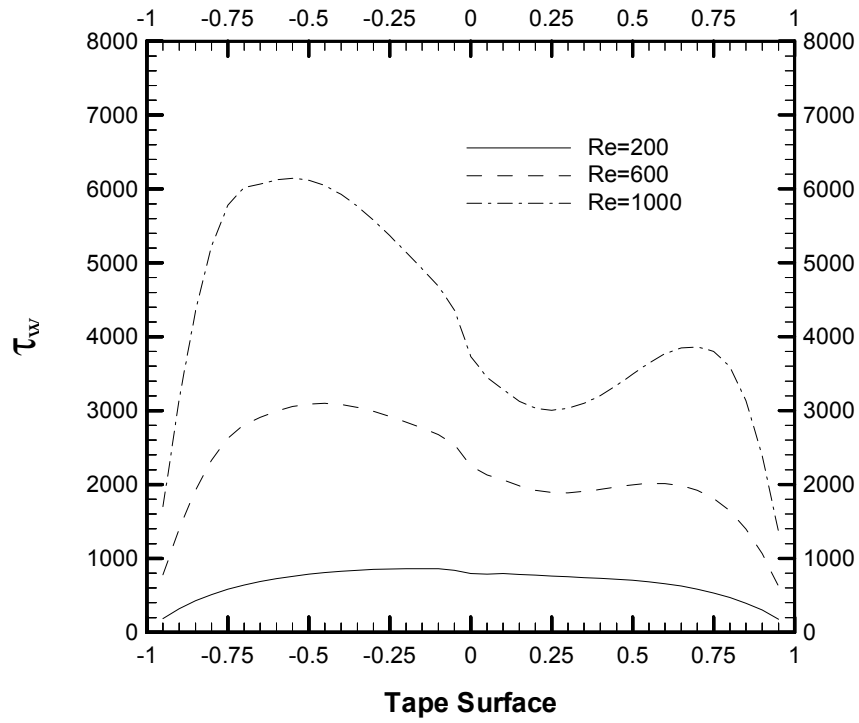


Fig. 4.4 Wall shear stress distribution for $y = 6$ and $Re = 200, 600$ and 1000

behavior is depicted in Fig. 4.4 for $y = 6$ and increasing flow rates ($Re = 200 \rightarrow 1000$). Furthermore, it is seen that the location of the maximum wall shear stress moves in the opposite direction of the tape twist as y decreases or Re increases, which is consistent with the axial velocity distributions shown in Figs. 4.1 and 4.2. Also, the second peak that develops with increasing swirl tends to be higher than the first peak at the tube wall, but is always lower on the tape surface. This is because the clockwise twisting of the tape results in a “push” effect on the $\theta = 180^\circ$ end and “draw” effect on the $\theta = 0$ end, which causes the axial velocity gradients to be greater on the “push” end than the “draw” end on the tape surface with a converse effect at the tube wall.

Another inference from Figs. 4.3 and 4.4 is that the flow Reynolds number has a greater impact on the change in the wall shear stress compared to that of the twist ratio. For a fixed Reynolds number ($Re = 800$ in Fig. 4.3), while the decrease in twist ratio changes the shear stress distribution significantly, the average value of the shear stress does not change appreciably. However, in Fig. 4.4, with a fixed twist ratio of $y = 6$, the local wall shear stress distribution as well as its average value increases drastically with increasing Re ($200 \rightarrow 1000$).

4.1.3 Friction factor

The predicted friction factors for different twist ratios y and flow rates Re are listed in Table 4.1. The values of fRe are based on the tube inside diameter or envelope, and are also graphed in Fig. 4.5 to show the variation with Re and y , along with the analytical solution for fully developed flows in a semi-circular tube (Sparron and Haji-Sheikh, 1966) given by

$$f Re = 42.23 \quad (4.8)$$

This result, it may be noted, represents the $y = \infty$, $\delta = 0$ case. As would be expected, for the same Re , the friction factor increases as y decreases or the severity of the tape twist increases. Also, at low Reynolds numbers, the results approach that for the $y = \infty$ limit, thereby implying that the twist ratio has a greater influence on the friction factor in the higher Reynolds numbers regime. The results are nevertheless slightly greater for each $y < \infty$, which suggests the higher pressure loss due to the longer helical flow path. The increase in pressure drop due to the twisted-tape insert can thus be considered to mainly consist of two parts: a straight tape insert that increases $fRe = 16$ to $fRe = 42.23$ over which is superimposed the higher friction due to the helical flow twisting and swirl at high Reynolds numbers.

To check the accuracy of the computational results, comparisons are made with previously reported (Manglik and Bergles, 1992) experimental data and correlation. The comparison with a typical set of data for $y = 6$ in the range $100 \leq Re \leq 1200$ is given in Fig. 4.6. It can be seen from the graph that the present results agree rather well with the experimental data, except for the relatively larger difference in the low Re region. This can be explained by the difference between the flow cross section geometry modeled for the numerical analysis and that encountered in practical situation. As described previously in Chapter 2 and schematically illustrated in Fig. 2.1, the tape in an actual tube has a finite thickness and is slightly curved. Consequently the two partitioned flow channels are different from a semi-circular cross section. Also, the fit between the tape edges and the tube wall is not tight enough so that leakage occurs in the flow path. All of these factors contribute to the differences seen in the friction factor results, particularly at low flow rates.

Finally, the predicted friction factor fRe is compared with the correlation suggested by Manglik and Bergles (1993a), which is based on the Swirl number (S_w) that was proposed to

Table 4.1 Fanning friction factors for different twist ratios (y) and flow rates (Re) for fully developed swirl flows in circular tube with twisted-tape inserts

Re	$y = 3$		$y = 6$		$y = 12$	
	Sw	fRe	Sw	fRe	Sw	fRe
20	13.03	43.20	8.44	42.54	5.82	42.38
50	32.59	43.28	21.10	42.55	14.56	42.38
100	65.17	43.97	42.20	42.63	29.11	42.39
200	130.3	46.80	84.40	43.32	58.23	42.64
400	260.6	53.02	168.8	46.13	116.5	44.11
600	391.0	57.49	253.2	49.23	174.7	45.68
800	521.3	64.70	337.6	54.30	232.9	47.42
1000	651.7	69.49	422.0	57.23	291.1	49.17
1200	782.0	75.16	506.4	59.97	349.4	50.88

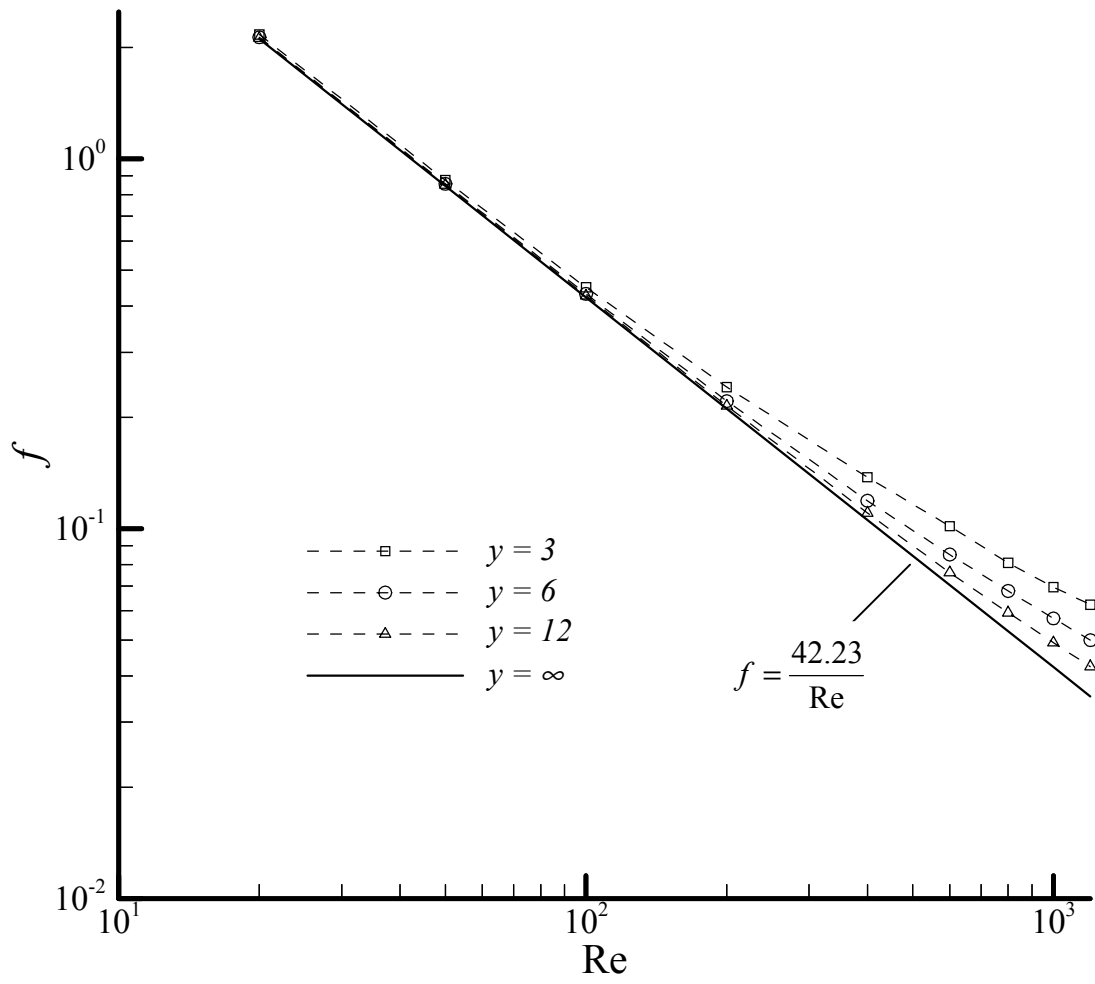


Fig. 4.5 Influence of the twist ratio y on friction factors

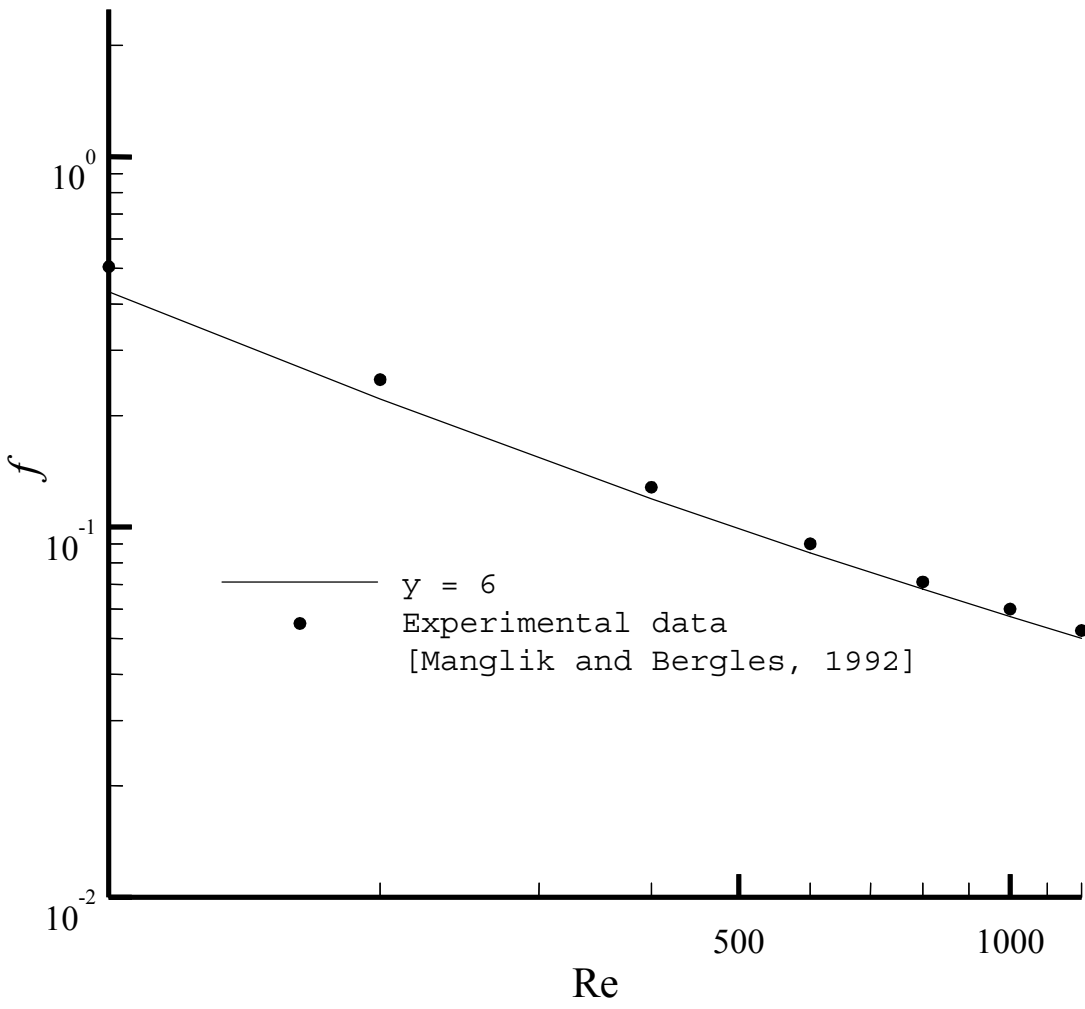


Fig. 4.6 Comparison of the computational friction factor results with experimental data of Magnlik and Bergles (1992)

scale the tape-induced swirl flows. It represents the interaction between the twisted tape's helical-curvature induced force, and the convective inertia and viscous forces expressed as

$$\frac{(\text{Centrifugal force})(\text{Convective force})}{(\text{Viscous force})^2} = \frac{(\rho V_s^2 / H)(\rho V_s^2 / D)}{(\mu V_s / D^2)^2} = \frac{\text{Re}_s^2}{y} \quad (4.9)$$

Here the reference velocity V_s is the actual swirl flow velocity at the tube wall, which directly influence the shear stress, and is given in terms of its axial and tangential velocity components as follows:

$$V_a = \frac{\dot{m}}{\rho A_c}, \quad V_t = \frac{\pi V_a}{2y}, \quad V_s = V_a \left[1 + \left(\frac{\pi}{2y} \right)^2 \right]^{1/2} \quad (4.10)$$

Furthermore, because the square of Reynolds number becomes very large in magnitude, the swirl parameter is redefined as

$$Sw = \frac{\text{Re}_s}{\sqrt{y}} = \frac{\text{Re}}{\sqrt{y}} \left[1 + \left(\frac{\pi}{2y} \right)^2 \right]^{1/2} \quad (4.11)$$

as previously expressed in Eq. (1.2). Thus, the empirical friction factor of Eq. (1.4), given by Manglik and Bergles (1993a), reduces to

$$(f \text{Re})_s = 42.23(1 + 10^{-6} Sw^{2.55})^{1/6} \quad (4.12)$$

for the case of a zero-thickness ($\delta = 0$) tape. The comparison with its predictions is graphed in Fig. 4.7, where the remarkable agreements (within $\pm 5\%$) is clearly evident. This striking result not only verifies the accuracy of the present computational simulations, but also establishes the unequivocal efficacy of the swirl parameter Sw of Eq. (4.11) in scaling and correlation the helical secondary flows generated by twisted-tape inserts.

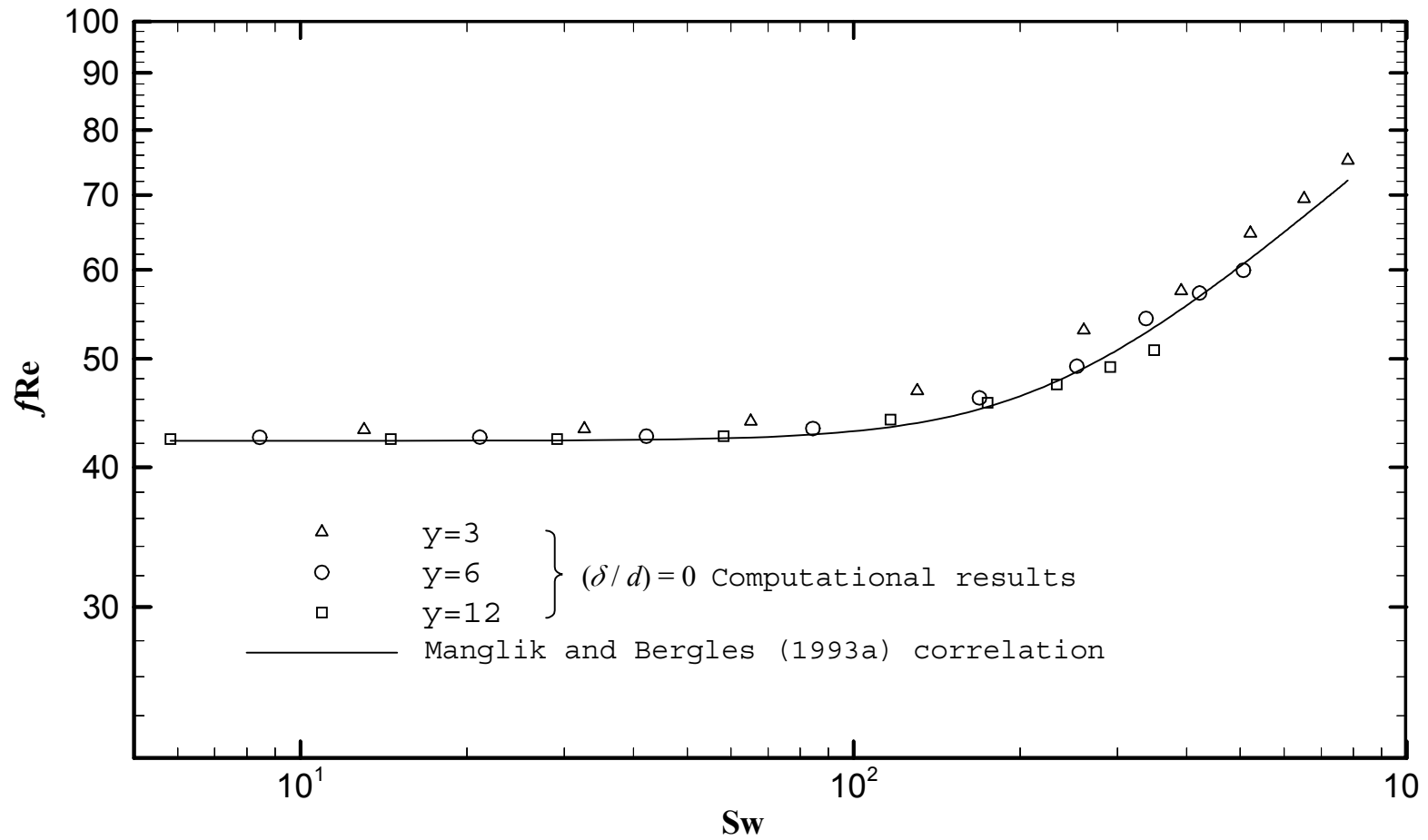


Fig. 4.7 Comparison of the computational fRe results with the correlation of Manglik and Bergles (1993a)

4.2 Heat Transfer

The temperature field of the fully developed laminar swirl flow is dependent on the velocity distributions and Prandtl number Pr and, therefore, is strongly influenced by the flow Reynolds number Re , twist ratio y and Prandtl number Pr . In the mean time, the variation of the fin efficiency of the twisted tape could change the thermal boundaries of the energy equation and consequently result in different temperature distributions. The influences of these factors on the temperature distributions can be illustrated by plotting the temperature profiles along with the stream function ψ for both Case 1 and Case 2, where the ratio of the local temperature to the mean temperature (T/T_m) is calculated and graphed in contour lines. The variations of Nusselt number with Re , y , and Pr are also graphed to show their influences on the heat transfer of the laminar swirl flow.

4.2.1 Temperature distribution

As discussed in Section 4.1.1, increasing Reynolds number Re or decreasing twist ratio y has essentially similar effects on the velocity distributions. The temperature distribution follows the same trends as well.

The influence of increasing Re , or the flow rate, on the temperature distributions is illustrated in Fig. 4.8 with a fixed twist ratio $y = 3$ and Prandtl number $Pr = 1$ for both Case 1 and Case 2. It can be seen that the temperature profiles for Case 1 are similar to that of the axial velocity. With the tape twisting in the clockwise direction along the flow path, the peak of the temperature contours shifts off-center in the anti-clockwise direction ($\bar{\theta} > 90^\circ$). As Re increases, a second flow re-circulation is formed near the $\bar{\theta} \approx 0$ flat tape surface. This vortex grows with Re and causes the temperature contours to curve up near the tape surface. When the second cell

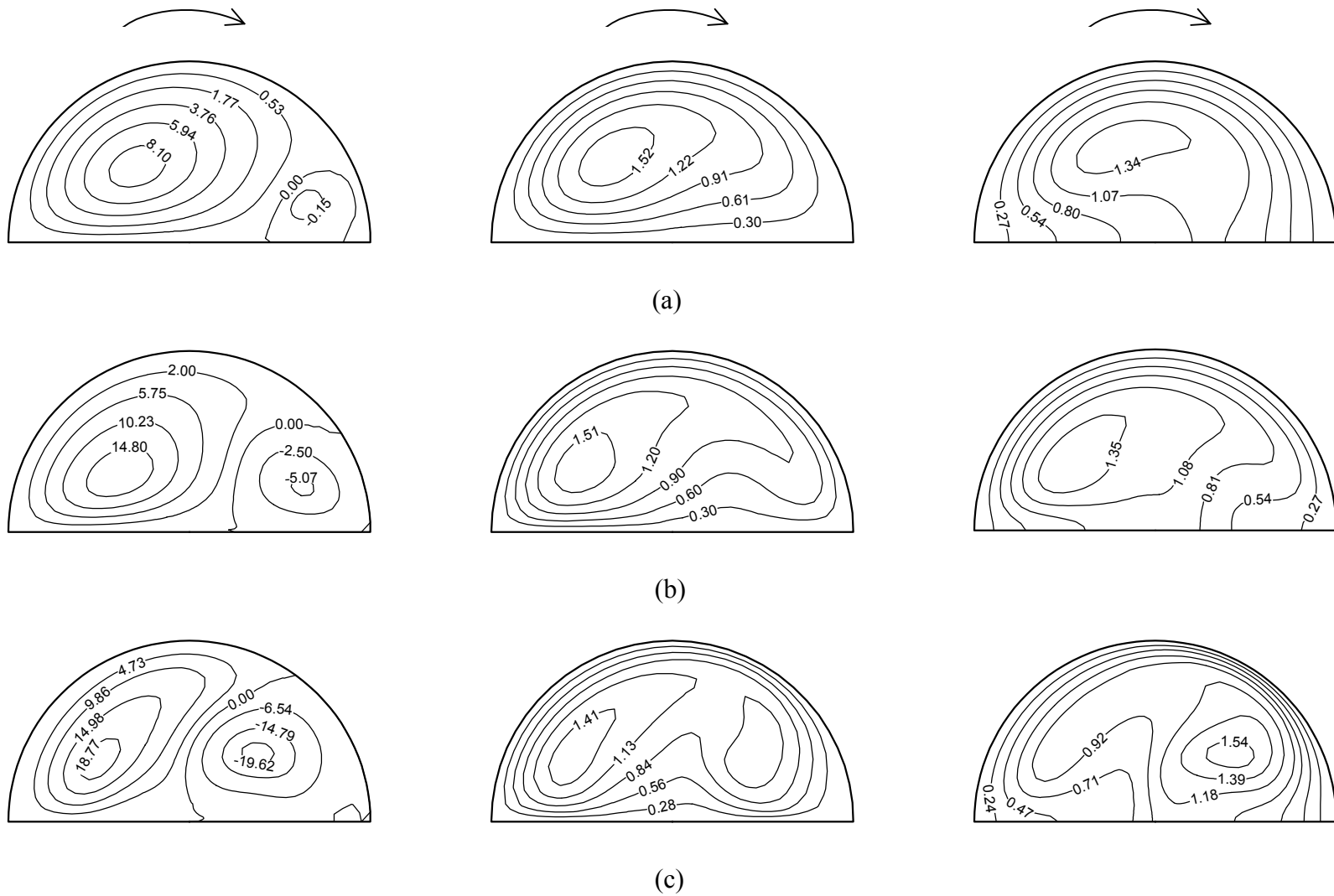


Fig. 4.8 Stream function and temperature distributions (Case 1 and 2) for $y = 3$, $Pr = 1$, and
 (a) $Re = 200$, (b) $Re = 600$, and (c) $Re = 1000$

grows large enough to occupy almost half the cross-section, the temperature contour lines are forced to split from the center and, thus, a second peak of temperature contours appears in the $\bar{\theta} < 90^\circ$ region. This swirl-induced temperature re-distribution is also reflected in the temperature profiles for Case 2. Because the tape is adiabatic in Case 2, the temperature contour lines are perpendicular to the flat tape surface and the second temperature peak is further away from the tape than Case 1.

The stream function distribution and the temperature contours in Fig. 4.9 shows the influence of y on the temperature field with a fixed flow rate $Re = 800$ and Prandtl number $Pr = 1$. The helical swirl flow that is generated by the curvature of the gently twisted tape ($y = 12$) is seen to form an anti-clockwise secondary circulation and thus force the temperature contour peak shift to the $\bar{\theta} > 90^\circ$ region. With y decreasing or the tape twisted more severely, a second vortex rotating in the clockwise direction is generated near the $\bar{\theta} \approx 0$ tape surface. These two counter-rotating vortices force the temperature contour lines to concave up till the second vortex grows strong enough to produce another temperature contour peak. This temperature re-distribution trend with decreasing y ($12 \rightarrow 3$) with fixed $Re (= 800)$ is similar to that seen in Fig. 4.8 for fixed $y (= 3)$ and increasing Re ($200 \rightarrow 1000$).

The influence of Prandtl number Pr on the temperature distribution is illustrated in Fig. 4.10, where the variations in ψ and (T / T_m) are graphed with $Pr = 1, 6,$ and 80 , for a fixed flow rate of $Re = 600$ and twist ratio $y = 6$. The Prandtl number is the ratio of the momentum diffusivity to the thermal diffusivity of the fluid flow. At low Prandtl number ($Pr = 1$), the convective energy transport is equivalent to the diffusive transport; accordingly, the temperature profile approximately matches the axial velocity profile. As Prandtl number increases ($1 \rightarrow 80$), the convective energy transport is strengthened to dominate the heat transfer in the flow field.

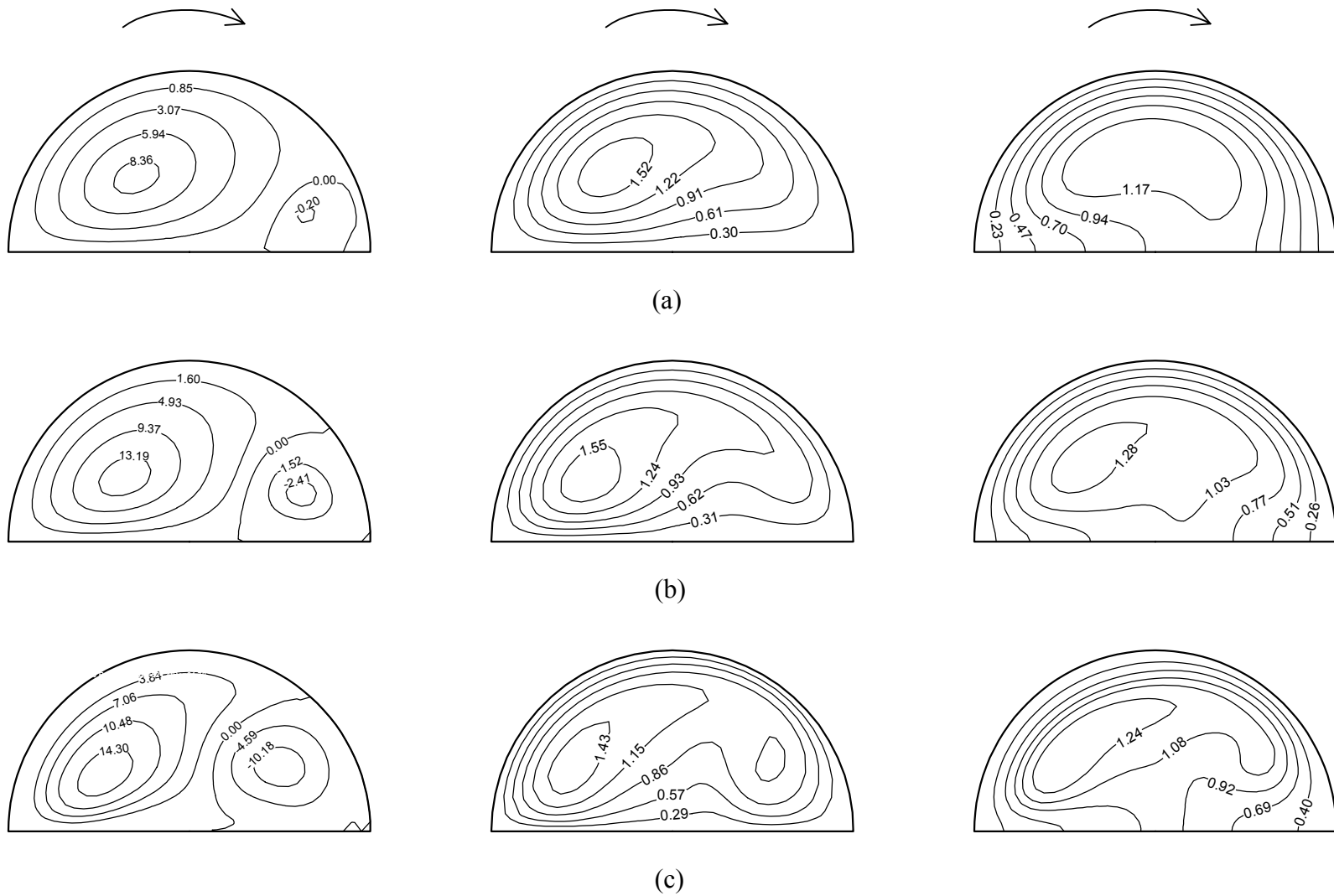


Fig. 4.9 Stream function and temperature distributions (Case 1 and 2) for $Re = 800$, $Pr = 1$, and
 (a) $y = 12$, (b) $y = 6$, and (c) $y = 3$

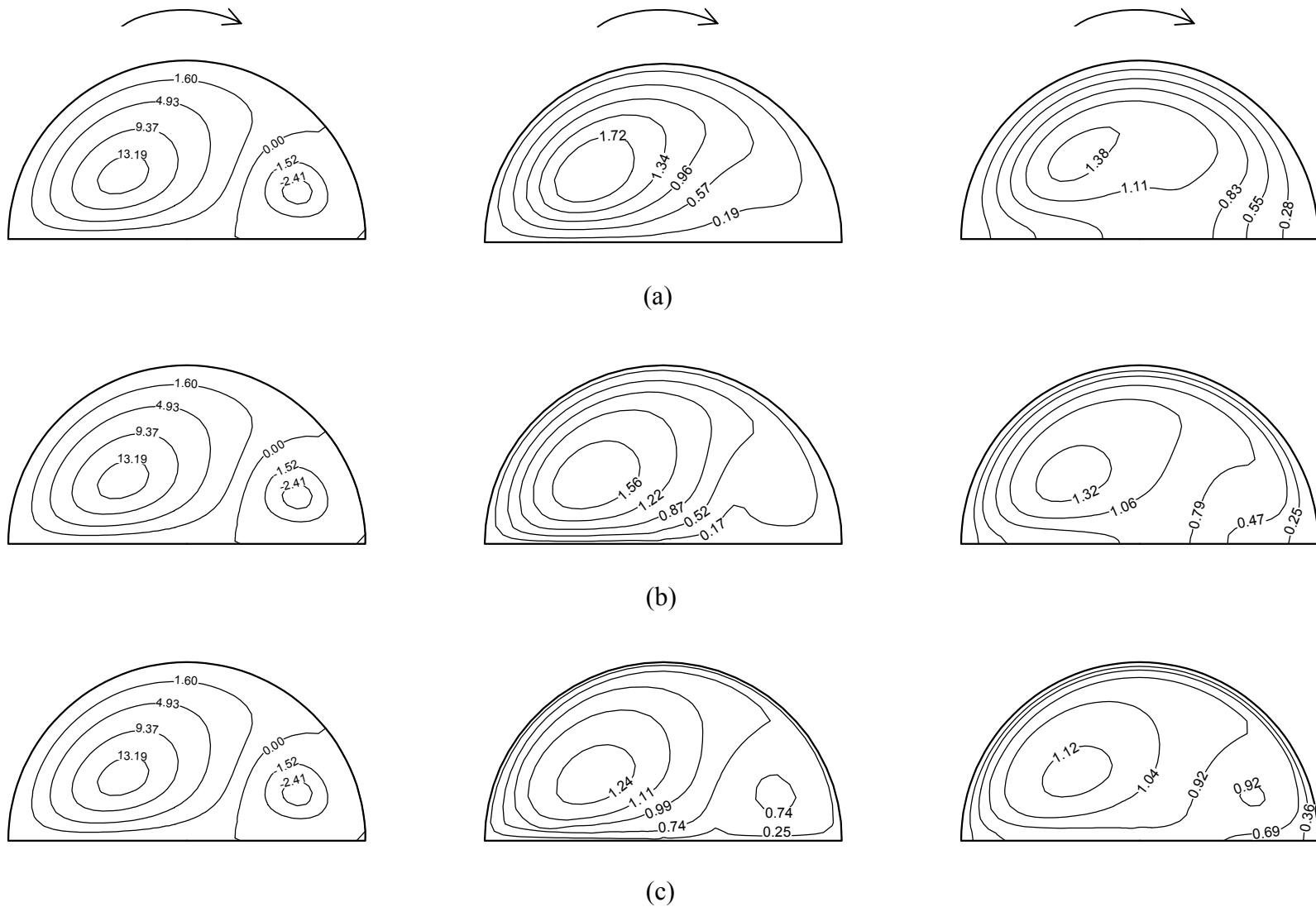


Fig. 4.10 Stream function and temperature distributions (Case 1 and 2) for $Re = 600$, $y = 6$, and
 (a) $Pr = 1$, (b) $Pr = 6$, and (c) $Pr = 80$

Although the velocity distribution does not change with Pr, the temperature field forms a second contour peak over the second velocity vortex.

4.2.2 Nusselt number

The predicted Nusselt number for various flow rate Re, twist ratio y , and Prandtl number Pr and for both Case 1 and Case 2 are given in Table 4.2 through 4.7. The values of Nu are based on the tube inside diameter, and are also graphed in Fig.4.11 and 4.12 to show the influences of twist ratio y and Prandtl number Pr on Nusselt numbers.

The variation of Nusselt number with Reynolds number at various twist ratios for Case 2 and UWT condition is shown in Fig. 4.11, with a fixed Prandtl number $Pr = 1$. The solid line in this graph corresponds to the analytical solution for fully developed laminar flow in a semi-circular tube given by

$$Nu_{y=\infty} = 4.612 \quad (4.13)$$

This result represents the $y=\infty, \delta = 0$ case, and is independent of Reynolds number and Prandtl number. The dashed lines correspond to several finite twist ratios ($y = 3, 6, \text{ and } 12$). Due to the existence of the secondary flow, the Nusselt number is influenced by the twist ratio y as well as the Reynolds number. For the same Re, the Nusselt number increases as y decreases or the severity of the tape twist increases. This is particularly significant at high Reynolds numbers. At low Reynolds numbers, the Nusselt numbers approach the analytical solution and do not change much with the twist ratio; thereby implying the twist ratio has a greater influence on the Nusselt number in the higher Reynolds number regime.

The variation of Nusselt number with Reynolds number is shown in Fig. 4.12 for a fixed twist ratio $y = 6$ and various Prandtl numbers for Case 2 and UWT condition, along with the

Table 4.2 Nusselt Numbers for Pr = 1 and Case 1

Re	y = 3		y = 6		y = 12	
	UWT	UHF	UWT	UHF	UWT	UHF
20	8.60	10.72	8.57	10.74	8.56	10.74
50	8.85	10.91	8.64	10.78	8.58	10.75
100	9.42	11.57	8.86	10.96	8.64	10.79
200	10.60	13.23	9.44	11.60	8.86	10.97
400	12.94	16.63	10.61	13.27	9.44	11.61
600	16.51	20.84	12.94	16.01	10.68	13.05
800	19.04	23.57	14.27	17.81	11.46	14.05
1000	21.03	24.52	15.46	19.43	12.22	15.05
1200	23.91	26.72	16.55	20.91	12.95	16.03

Table 4.3 Nusselt Numbers for Pr = 1 and Case 2

Re	y = 3		y = 6		y = 12	
	UWT	UHF	UWT	UHF	UWT	UHF
20	4.71	5.48	4.61	5.4	4.61	5.5
50	5.11	5.81	4.77	5.52	4.66	5.55
100	5.76	6.35	5.14	5.73	4.8	5.66
200	6.67	7.33	5.77	6.35	5.14	5.73
400	8.21	8.99	6.66	7.3	5.77	6.35
600	10.45	11.4	7.39	8.08	6.31	6.9
800	12.82	13.55	9.21	10.11	7.36	8.11
1000	15.14	15.68	10.77	11.78	8.28	9.09
1200	17.37	18.2	12.39	13.35	9.32	10.2

Table 4.4 Nusselt Numbers for Pr = 6 and Case 1

Re	y = 3		y = 6		y = 12	
	UWT	UHF	UWT	UHF	UWT	UHF
20	8.79	10.86	8.66	10.78	8.59	10.75
50	9.16	11.34	8.87	10.96	8.71	10.81
100	10.16	12.70	9.19	11.38	8.88	10.97
200	13.30	16.76	10.21	12.77	9.20	11.40
400	19.47	24.59	13.42	16.90	10.23	12.79
600	26.60	33.25	19.51	23.83	13.94	16.89
800	30.93	38.20	22.32	27.48	15.92	19.33
1000	32.73	37.52	24.60	30.57	17.82	21.70
1200	44.39	46.50	26.59	33.30	19.53	23.86

Table 4.5 Nusselt Numbers for Pr = 6 and Case 2

Re	y = 3		y = 6		y = 12	
	UWT	UHF	UWT	UHF	UWT	UHF
20	5.82	6.30	5.18	5.73	4.80	5.54
50	6.71	7.30	6.06	6.55	5.38	5.88
100	7.42	8.19	6.70	7.30	6.06	6.55
200	8.67	9.73	7.40	8.18	6.70	7.30
400	13.00	14.42	9.92	10.96	7.39	8.18
600	18.72	19.80	12.68	13.55	9.49	10.23
800	22.44	23.39	15.79	16.94	11.70	12.50
1000	25.84	26.29	18.74	19.50	14.35	15.20
1200	30.02	30.37	22.06	22.74	15.88	16.74

Table 4.6 Nusselt Numbers for Pr = 80 and Case 1

Re	y = 3		y = 6		y = 12	
	UWT	UHF	UWT	UHF	UWT	UHF
20	10.79	12.80	9.72	11.75	9.06	11.10
50	15.41	17.41	12.50	14.50	10.15	12.18
100	22.89	25.12	17.28	19.25	12.53	14.53
200	38.90	42.26	25.79	28.00	17.33	19.30
400	57.75	63.64	42.07	45.56	25.84	28.06
600	56.28	64.86	50.05	54.48	35.10	38.24
800	63.29	70.61	53.53	59.27	41.48	45.23
1000	59.30	63.41	54.86	62.26	46.56	50.59
1200	68.26	69.40	55.76	64.77	50.02	54.49

Table 4.7 Nusselt Numbers for Pr = 80 and Case 2

Re	y = 3		y = 6		y = 12	
	UWT	UHF	UWT	UHF	UWT	UHF
20	7.93	8.81	7.277	8.061	6.82	7.47
50	10.08	10.95	8.227	9.139	7.43	8.258
100	13.65	14.32	10.09	10.95	7.88	8.8
200	19.45	19.87	13.67	14.34	10.08	10.95
400	28.02	28.22	19.47	19.89	16.77	17.41
600	38.22	38.49	28.92	29.22	20.12	20.59
800	49.5	49.57	32.82	33.1	26.74	26.99
1000	57.92	58.18	40.17	41.19	31.92	32.13
1200	67.94	68.15	45.08	45.28	35.66	35.83

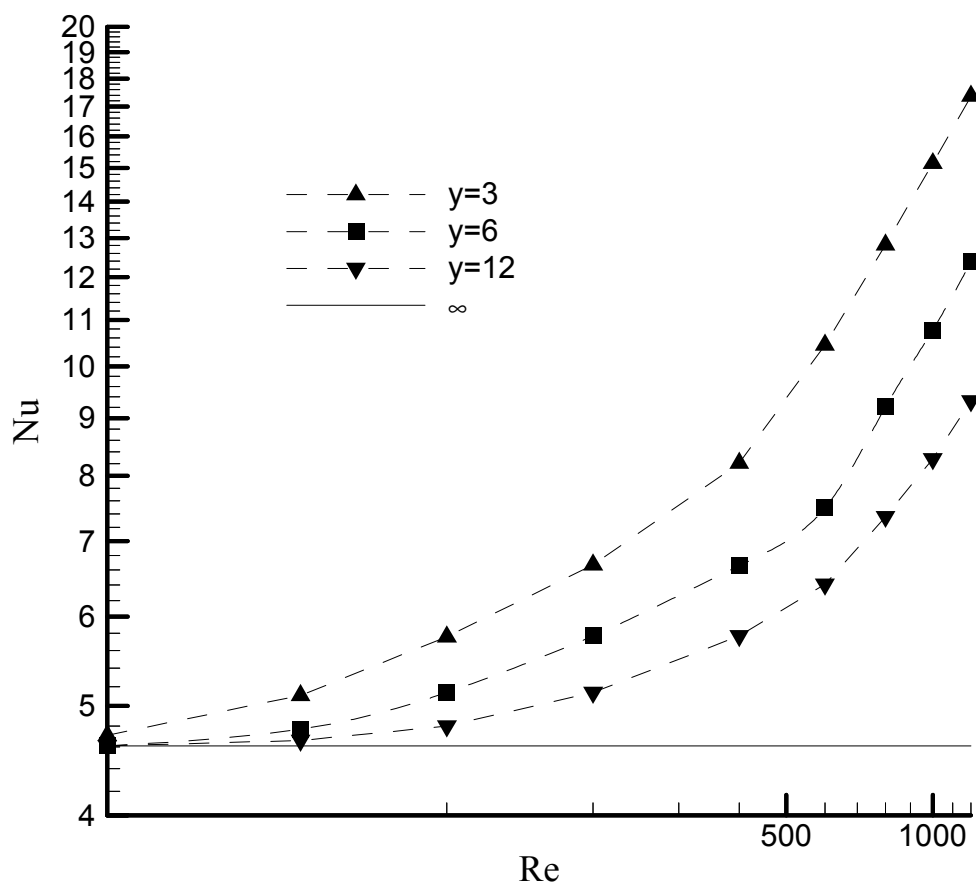


Fig. 4.11 Influence of twist ratio y on Nusselt numbers at $Pr = 1$ for UWT and Case 2

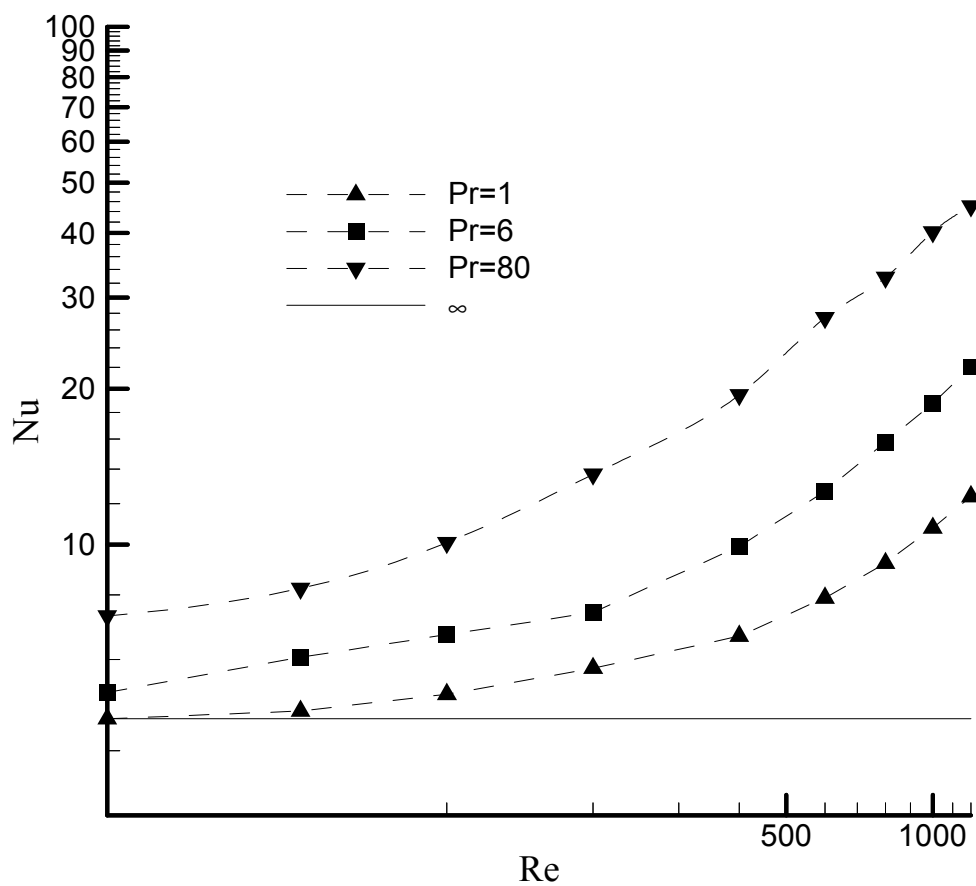


Fig. 4.12 Influence of Pr on Nusselt numbers at $y = 6$ for UWT and Case 2

analytical solution for the fully developed laminar flow in a semi-circular tube given by Eq. (4.13). It's seen that, for the same Re, the Nusselt number increases as Pr increases. This is particularly significant at high Reynolds numbers. At low Reynolds numbers, the Nusselt numbers approach the analytical solution and do not change much with the Prandtl number; thereby implying the Prandtl number has a greater influence on the Nusselt number in the higher Reynolds number regime.

The variation of the ratio of the computational Nusselt number to that for $y = \infty$ limit ($Nu / Nu_{y=\infty}$) with different values of $SwPr^{0.391}$ is compared with the empirical correlation suggested by Manglik and Bergles (1993a) for Case 2 and UWT boundary condition. Since assumptions are made in the present study that the fluid properties are constant and the buoyancy effect is neglected, the Nusselt number correlation of Eq. (1.5), given by Manglik and Bergles (1993a), reduces to

$$Nu = 4.612 \left(1 + 6.413 \times 10^{-9} (Sw \cdot Pr^{0.391})^{3.835} \right)^{0.2} \quad (4.14)$$

The comparison with the predicted Nusselt numbers is graphed in Fig. 4.13. It is seen that the trend followed by the numerical results is slightly different from that by the correlation. According to the correlation, the Nusselt numbers level off when $Sw \cdot Pr^{0.391}$ is less than 100; after that the values of Nusselt number increase at a constant rate. The prediction of the present study, however, shows that Nusselt number starts to increase at low $Sw \cdot Pr^{0.391}$. Therefore the difference between the correlation and numerical method is relatively large around $Sw \cdot Pr^{0.391} = 100$ region. This could be explained by several reasons. In the experiment setup, the adiabatic flat wall condition was not ideally achieved since the twisted tape was not deliberately insulated so as for additional temperature gradient at the tape surface. Also, the correlation took into consideration fluid property variation, while the present study assumes constant properties.

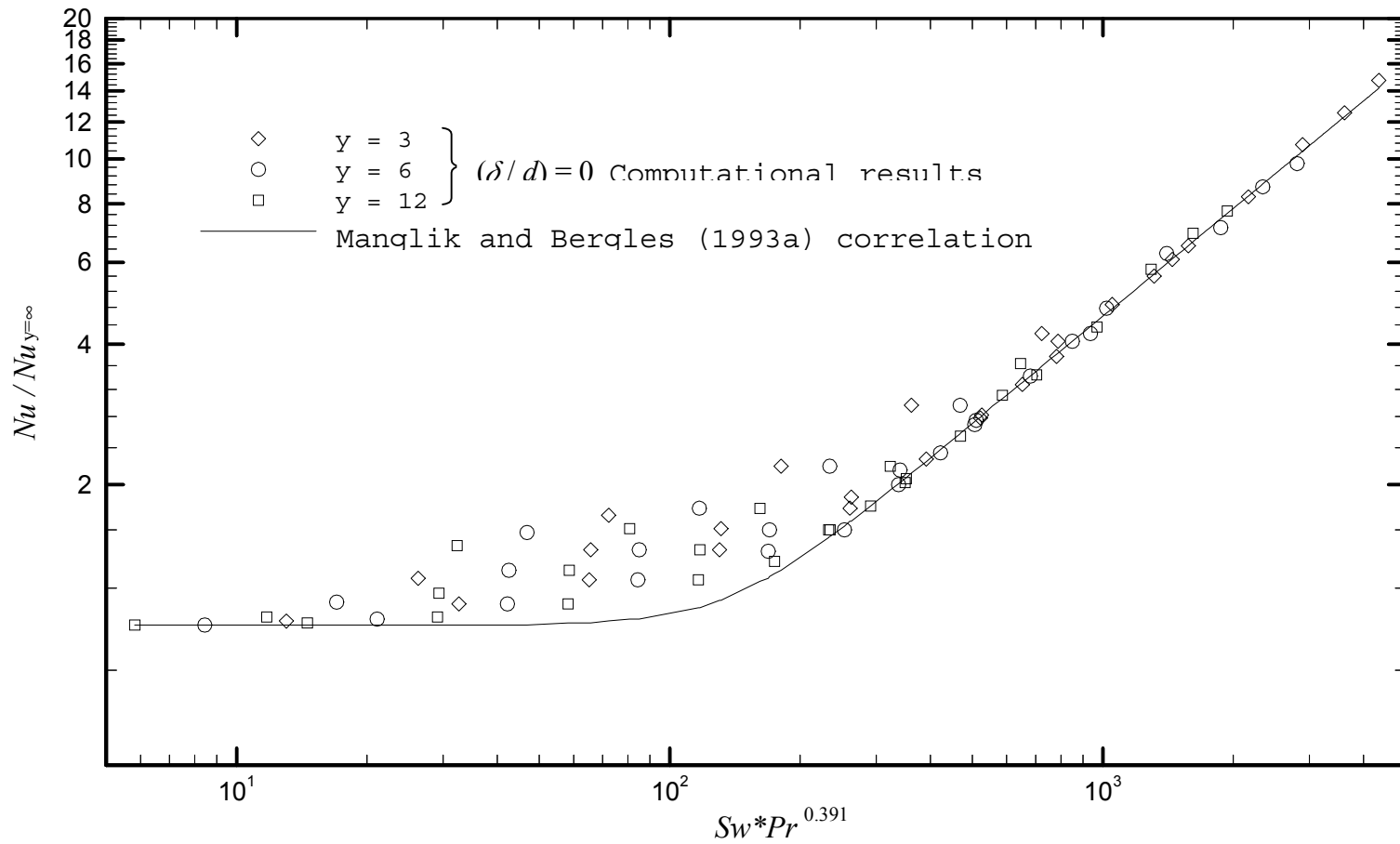


Fig. 4.13 Comparison of computational Nu results with correlation of Manglik and Bergles (1993a)

Finally for high $Sw*Pr^{0.391}$ the secondary flow distributes heat evenly and thus causes large temperature gradients at the tube wall, too large to be precisely described by the finite control method used in this study. A more robust scheme should be adopted that takes property variation and buoyancy force into consideration.

CHAPTER 5. CONCLUSIONS AND RECOMMENDATIONS

5.1 Conclusions

The main conclusions that can be drawn from this computational study are as follows:

- The fully developed laminar swirl flow induced by twisted-tape inserts can be modeled by a semi-circular flow with an axially helical geometry.
- The Finite Control Volume Method can be applied to discretize the governing differential equations.
- The twisted-tape-curvature-induced centrifugal forces promote the secondary circulation in the flow cross section. As Re increases or y decreases, the single-cell vortex structure develops into a double-cell structure with two counter-rotating helical vortices.
- Due to the tape twist, the highest local shear stress on the tape surface is on the side of the primary vortex, and the highest local shear stress at the tube wall is on the side of the secondary vortex.
- The average wall shear stress does not change much with the twist ratio y ; therefore, Re has a greater influence on the friction factor than y .
- The computational results of friction factors agree very well (within $\pm 5\%$) with the available experimental data and predictive correlation.

- The temperature distributions in the flow field are seen to be strongly influenced by Pr , as well as Re and y .
- The computational predictions of Nusselt numbers indicate that significant augmentation in heat transfer can be obtained at high Reynolds number, high Prandtl number, and low twist ratio.
- The numerical results are again in good agreement (within $\pm 5\%$) with the available experimental-data-based correlation in the fully developed swirl regime. In the early swirl onset regime, however, the computations require some additional resolution.

5.2 Recommendations

The quantitative disagreement between the predicted results and the Manglik and Bergles (1993a) correlation for Nusselt numbers exposes somewhat the inadequacy of simplifications and assumptions in modeling the twisted-tape flow and heat transfer problem. In practice, the twisted-tape always has some fin efficiency, which may significantly change the thermal boundary conditions. Also, the buoyancy effect may not have been neglected because the natural convection does exist in the actual flow fluid. Future work needs to take these factors into considerations.

BIBLIOGRAPHY

Anderson, D.A., Tannehill, J.C., and Pletcher, R.H. (1984). "Computational Fluid Mechanics and Heat Transfer", Hemisphere Pub. Corp., Washington; McGraw-Hill, NY.

Bergles, A.E. (1998). Techniques to augment heat transfer. In "Handbook of Heat Transfer" (W. M. Rohsenow, J.P. Hartnett, and Y.I. Cho, Eds.), 3rd ed., ch. 11. McGraw-Hill, New York.

Date, A.W. (1974). Prediction of fully developed flow in a tube containing a twisted tape. *International Journal of Heat and Mass Transfer* **17**, 845-859.

Donevski, B., and Kulesza, J. (1978). Resistance coefficients for laminar and turbulent flow in swirling ducts. *Archiwum Termodynamiki I Spalania* **9**(3), 497-506 (in Polish).

DuPlessis, J.P., and Kröger, D.G. (1984). Friction factor prediction for fully developed laminar twisted-tape flow. *International Journal of Heat and Mass Transfer* **27**, 2095-2100.

DuPlessis, J.P., and Kröger, D.G. (1987). Heat transfer correlation for thermally developing laminar flow in a smooth tube with a twisted-tape insert. *International Journal of Heat and Mass Transfer* **30**, 509-515.

Gottlieb, D. and Orszag, S.A. (1977). "Numerical Analysis of Spectral Methods: Theory and Applications", Society for Industrial and Applied Mathematics, Philadelphia.

Hong, S.W., and Bergles, A.E. (1976). Augmentation of laminar flow heat transfer in tubes by means of twisted-tape inserts. *Journal of Heat Transfer* **98**, 251-256.

Jaluria, Y. (1980). "Natural Convection: Heat and Mass Transfer", 1st ed., Pergamon Press, NY.

Manglik, R.J. and Bergles, A.E. (1991). "Heat Transfer enhancement of Intube Flows in Process Heat Exchangers by Means of Twisted-Tape Inserts". Heat Transfer Laboratory Report No. HTL-8, Rensselaer Polytechnic Institute, Troy, NY.

Manglik, R.M., and Bergles, A.E. (1992). Heat transfer enhancement and pressure drop in viscous liquid flows in isothermal tubes with twisted-tape inserts. *Wärme- und Stoffübertragung* **27**, 249-257.

Manglik, R.M., and Bergles, A.E. (1993a). Heat transfer and pressure drop correlations for twisted-tape inserts in isothermal tubes: Part I - Laminar flows. *Journal of Heat Transfer* **115**, 881-889.

- Manglik, R.M., and Bergles, A.E. (1993b). Heat transfer and pressure drop correlations for twisted-tape inserts in isothermal tubes: Part II - Transition and turbulent flows. *Journal of Heat Transfer* **115**, 890-896.
- Manglik, R.M., and Ranganathan, C. (1997). Visualization of swirl flows generated by twisted-tape inserts in circular tubes. In "Experimental Heat Transfer, Fluid Mechanics and Thermodynamics 1997", (M. Giot et al., Eds.), pp. 1631-1636. Edzioni ETFS, Pisa, Italy.
- Manglik, R.M., Maramraju, S., and Bergles, A.E. (2001). The scaling and correlation of low Reynolds number swirl flows and friction factors in circular tubes with twisted-tape inserts. *Journal of Enhanced Heat Transfer* **8** (in press).
- Manglik, R.M., and Bergles, A.E. (2002). Swirl flow heat transfer and pressure drop with twisted-tape inserts. In "Advances in Heat Transfer", **Vol. 36**, Academic, New York (in press).
- Marner, W.J., Bergles, A.E., and Chenoweth, J.M. (1983). On the Presentation of Performance Data for Enhanced Tubes used in Shell-and-Tube Heat Exchangers, *Journal of Heat Transfer*, **105**, 358-365.
- Marner, W.J., and Bergles, A.E. (1989). Augmentation of highly viscous laminar heat transfer inside tubes with constant wall temperature. *Experimental Thermal and Fluid Science* **2**, 252-267.
- Nandakumar, K., and Masliyah, J.H. (1986). Swirling flow and heat transfer in coiled and twisted pipes. In "Advances in Transport Processes" (A.S. Mujumdar and R.A. Mashelkar, Eds.), pp. 40-112, Wiley Eastern, New Delhi.
- Patankar, S.V. (1980). "Numerical Heat Transfer and Fluid Flow", McGraw-Hill, NY.
- Seymour, E.V. (1966). Fluid flow through tubes containing twisted tapes. *The Engineer* **222**, 634-642.
- Smith, G.D. (1985). "Numerical Solution of Partial Differential Equations: Finite Difference Methods", 3rd ed. Oxford University Press, New York.
- Smithberg, E., and Landis, F. (1964). Friction and forced convection heat transfer characteristics in tubes with twisted tape swirl generators. *Journal of Heat Transfer* **86**, 39-49.
- Watanabe, K., Taira, T., and Mori, Y. (1983). Heat transfer augmentation in tubular flow by twisted tapes at high temperatures and optimum performance. *Heat Transfer - Japanese Research* **12**(3), 1-31.
- Webb, R.L. (1994). "Principles of Enhanced Heat Transfer." Wiley, New York.
- Zienkiewicz, O.C. and Taylor, R.C. (1991), "The Finite Element Method", 4th ed. McGraw-Hill, New York.

Appendix A. Mean Velocity and Friction Factor

The mean flow velocity is defined as

$$\bar{w}_m = \frac{1}{A_c} \int_{A_c} \bar{w} dA_c = \frac{2}{\pi R^2} \int_0^R \int_0^\pi \bar{w} r' d\theta' dr' \quad (\text{A.1})$$

The dimensionless variables are introduced in Chapter 2 as follows

$$w = \frac{\bar{w}}{v/R}, \quad r = \frac{r'}{R}, \quad \text{and} \quad \theta = \theta'$$

Thus

$$w_m = \frac{\bar{w}_m}{v/R} = \frac{2}{\pi} \int_0^1 \int_0^\pi w r d\theta dr \quad (\text{A.2})$$

The Reynolds number is defined as

$$\text{Re} = \frac{\bar{w}_m D}{v} = 2 \frac{\bar{w}_m}{v/R} = 2w_m \quad (\text{A.3})$$

This relation shows that once the Reynolds number is input, the dimensionless mean velocity is known. The problem thereafter is to solve the velocity distribution. When solving the axial momentum equation, the normalized velocity \hat{w} ($= w / G$) is firstly solved, where G is the pressure drop constant and defined as

$$G = \frac{(-d\bar{p}/dz)}{\rho v^2 / R^3}$$

After \hat{w} is obtained, G can be calculated as

$$G = \frac{w_m}{\hat{w}_m} = \frac{\text{Re}/2}{\frac{2}{\pi} \int_0^1 \int_0^\pi \hat{w} r d\theta dr} = \frac{\pi \text{Re}}{4 \int_0^1 \int_0^\pi \hat{w} r d\theta dr} \quad (\text{A.4})$$

From a force balance over an elemental duct segment of length dz , the average wall shear stress is

$$\tau_w = \frac{A_c}{P_w} \left(\frac{d\bar{p}}{dz} \right) = \frac{R}{2} \left(\frac{\pi}{\pi + 2} \right) \left(\frac{d\bar{p}}{dz} \right) \quad (\text{A.5})$$

where

$$A_c = \frac{\pi R^2}{2} \quad \text{and} \quad P_w = (\pi + 2)R$$

The fanning friction factor is defined as

$$f = \frac{\tau_w}{\frac{1}{2} \rho \bar{w}_m^2} \quad (\text{A.6})$$

Substitution of τ_w and \bar{w}_m yields

$$f = \frac{G}{w_m^2} \left(\frac{\pi}{\pi + 2} \right) \quad \text{or} \quad f \text{ Re} = \frac{4G}{\text{Re}} \left(\frac{\pi}{\pi + 2} \right) \quad (\text{A.7})$$

Note this is the same result from another definition of f :

$$f = \frac{D_h}{2\rho\bar{w}_m^2} \left(-\frac{d\bar{p}}{dz} \right) \quad (\text{A.8})$$

Therefore Eq. (A7) is based on the hydraulic diameter d_h , and can be reduced to the following equation

$$f \text{ Re} = \frac{4G}{\text{Re}} \quad (\text{A.9})$$

which is based on the tube inside diameter d .

Appendix B. Mean temperature and Nusselt number

The mean flow temperature is defined as

$$\bar{T}_m = \frac{1}{A_C \bar{w}_m} \int \bar{w} \bar{T} dA_C \quad (\text{B.1})$$

The dimensionless temperature is introduced as

$$T = \frac{\alpha(T_w - \bar{T})}{\bar{w}_m R^2 (d\bar{T}_m / dz')} \quad \text{and} \quad T_m = \frac{\alpha(T_w - \bar{T}_m)}{\bar{w}_m R^2 (d\bar{T}_m / dz')}$$

Substitution of these expressions into Eq. (B.1) produces

$$T_m = \frac{2}{\pi \bar{w}_m} \int_0^1 \int_0^\pi w T r d\theta dr \quad (\text{B.2})$$

After the temperature distribution is determined, the Nusselt number can be evaluated in terms of the mean temperature. From an energy balance over an elemental duct segment of length dz' ,

$$q_w'' P_h dz' = \dot{m} c_p d\bar{T}_m$$

where

$$\dot{m} = \rho \bar{w}_m \frac{\pi R^2}{2}$$

Thus

$$q_w'' = \frac{\rho \bar{w}_m c_p \pi R^2}{2 P_h} \frac{d\bar{T}_m}{dz'} \quad (\text{B.3})$$

From Newton's Cooling Law, the heat transfer coefficient is

$$h = \frac{q_w''}{T_w - \bar{T}_m} = \frac{\rho c_p \bar{w}_m \pi R^2}{2(T_w - \bar{T}_m) P_h} \frac{d\bar{T}_m}{dz'} \quad (\text{B.4})$$

The Nusselt number thus can be calculated as

$$\begin{aligned}
 Nu &= \frac{hD}{k} = \frac{2hR}{k} \\
 &= \frac{\bar{w}_m R^2 (d\bar{T}_m / dz')}{(k / \rho c_p)(T_w - \bar{T}_m)} \frac{\pi R}{P_h} \\
 &= \frac{1}{T_m} \frac{\pi R}{P_h}
 \end{aligned}$$

where P_h is the hydraulic peripherals

$$P_h = \begin{cases} (\pi + 2)R, & \text{for Case 1} \\ \pi R, & \text{for Case 2} \end{cases}$$

Therefore, the Nusselt numbers can be calculated from the following equations:

$$Nu = \begin{cases} \frac{1}{T_m} \frac{\pi}{\pi + 2}, & \text{for Case 1} \\ \frac{1}{T_m}, & \text{for Case 2} \end{cases} \quad (\text{B.5})$$

Appendix C. Discretization of Governing Equations

The general different equation is given in Section 2.2.4 as follows

$$\frac{1}{r} \frac{\partial}{\partial r} \left(r \frac{\partial \phi}{\partial r} \right) - \frac{1}{r} \lambda \frac{\partial \phi}{\partial r} + \frac{1}{r} \beta \frac{\partial^2 \phi}{\partial r^2} - \frac{1}{r} \mu \frac{\partial \phi}{\partial \theta} + S_\phi = 0 \quad (2.19)$$

where λ , β , μ , and S_ϕ are given in Table 1 for each dependent variable.

The continuity equation can be rewritten as

$$\frac{1}{r} \frac{\partial}{\partial r} \left(\frac{\partial \psi}{\partial r} \right) + \frac{1}{r} \frac{\partial}{\partial \theta} \left(-\frac{\partial \psi}{\partial \theta} \right) = 0$$

i.e.
$$\frac{1}{r} \frac{\partial}{\partial r} (\lambda) + \frac{1}{r} \frac{\partial}{\partial \theta} (\mu) = 0 \quad (C.1)$$

Combining Eqs. (2.19) and (C.1) yields

$$\frac{1}{r} \frac{\partial}{\partial r} \left(\lambda \phi - r \frac{\partial \phi}{\partial r} \right) + \frac{1}{r} \frac{\partial}{\partial \theta} \left(\mu \phi - \beta \frac{\partial \phi}{\partial \theta} \right) = S_\phi \quad (C.2)$$

Introducing a term *total flux*, which is the sum of convective and diffusive terms, by defining

$$J_r = \lambda \phi - r \frac{\partial \phi}{\partial r} \quad \text{and} \quad J_\theta = \mu \phi - \beta \frac{\partial \phi}{\partial \theta} \quad (C.3)$$

Eq. (C3) reduces to

$$\frac{1}{r} \frac{\partial J_r}{\partial r} + \frac{1}{r} \frac{\partial J_\theta}{\partial \theta} = S_\phi \quad (C.4)$$

Integrating this equation over the control volume shown in Fig. C.1, we have

$$\int_{\theta_e}^{\theta_w} \int_{r_x}^{r_n} \frac{1}{r} \frac{\partial J_r}{\partial r} r d\theta dr + \int_{\theta_e}^{\theta_w} \int_{r_x}^{r_n} \frac{1}{r} \frac{\partial J_\theta}{\partial \theta} r d\theta dr = \int_{\theta_e}^{\theta_w} \int_{r_x}^{r_n} S r d\theta dr$$

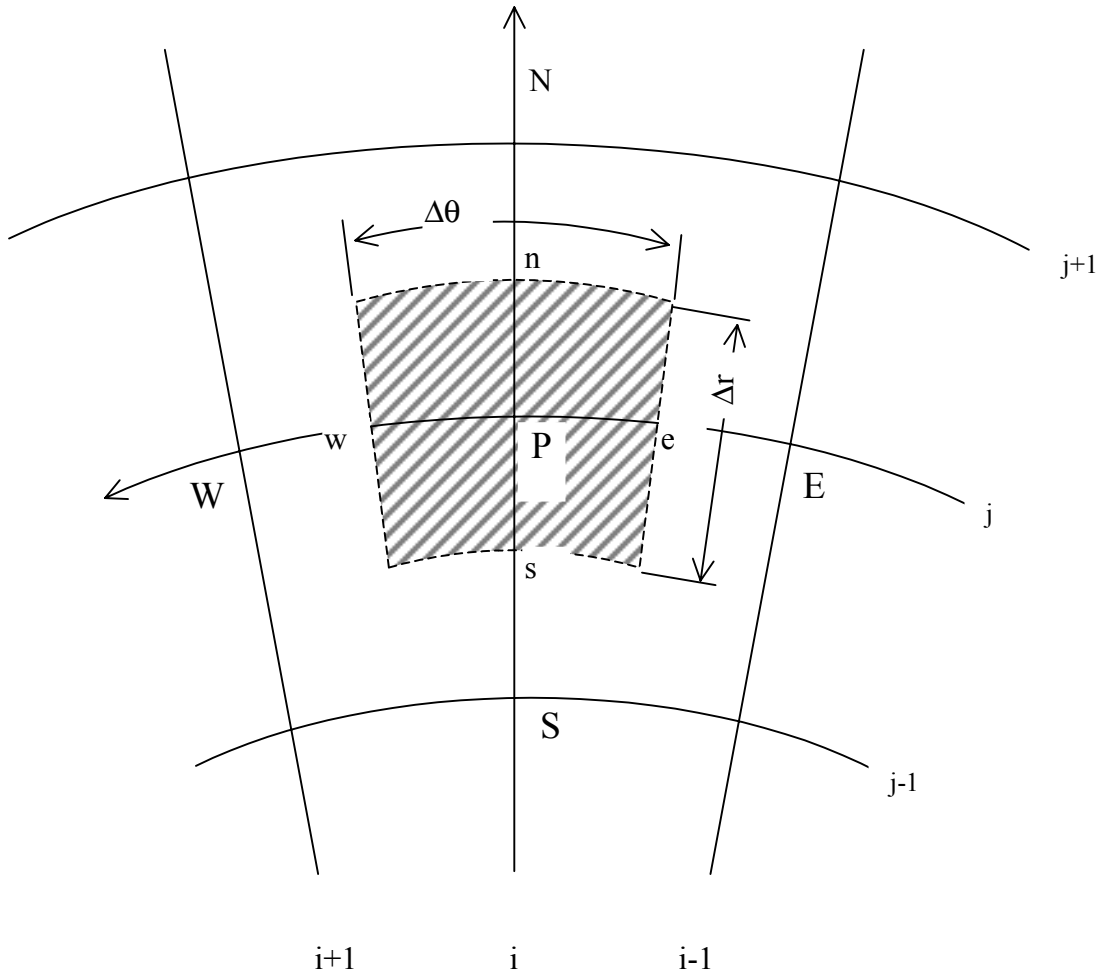


Fig. C.1 Finite Control Volume

which can be re-written as

$$(J_r|_n - J_r|_s) \cdot \Delta\theta + (J_\theta|_w - J_\theta|_e) \cdot \Delta r = S \cdot r \cdot \Delta r \cdot \Delta\theta \quad (\text{C.5})$$

Substituting Eq.(C.3) produces

$$\begin{aligned} & \left\{ \left[\lambda_n \phi_n - r_n \left(\frac{\partial \phi}{\partial r} \right)_n \right] - \left[\lambda_s \phi_s - r_s \left(\frac{\partial \phi}{\partial r} \right)_s \right] \right\} \Delta\theta \\ & + \left\{ \left[\mu_w \phi_w - \beta_w \left(\frac{\partial \phi}{\partial \theta} \right)_w \right] - \left[\mu_e \phi_e - \beta_e \left(\frac{\partial \phi}{\partial \theta} \right)_e \right] \right\} \Delta r = S \cdot r \cdot \Delta r \cdot \Delta\theta \end{aligned} \quad (\text{C.6})$$

The diffusive term must be expressed with the central difference schemes, as follows

$$\begin{aligned} \left(\frac{\partial \phi}{\partial r} \right)_n &= \frac{\phi_N - \phi_P}{\Delta r}, & \left(\frac{\partial \phi}{\partial r} \right)_s &= \frac{\phi_P - \phi_S}{\Delta r} \\ \left(\frac{\partial \phi}{\partial \theta} \right)_e &= \frac{\phi_P - \phi_E}{\Delta \theta}, & \left(\frac{\partial \phi}{\partial \theta} \right)_w &= \frac{\phi_W - \phi_P}{\Delta \theta} \end{aligned}$$

The convective terms can be interpreted by several schemes; only central differencing and upwind scheme are described in detail.

Central Differencing Scheme

Define

$$\begin{cases} F_n = \lambda_n \cdot \Delta\theta \\ F_s = \lambda_s \cdot \Delta\theta \\ F_w = \mu_w \cdot \Delta r \\ F_e = \mu_e \cdot \Delta r \end{cases} \quad \text{and} \quad \begin{cases} D_n = r_n \cdot \Delta\theta / \Delta r \\ D_s = r_s \cdot \Delta\theta / \Delta r \\ D_w = \beta_w \cdot \Delta r / \Delta\theta \\ D_e = \beta_e \cdot \Delta r / \Delta\theta \end{cases}$$

and let

$$\phi_n = \frac{\phi_N + \phi_P}{2}, \phi_s = \frac{\phi_S + \phi_P}{2}, \phi_w = \frac{\phi_W + \phi_P}{2}, \phi_e = \frac{\phi_E + \phi_P}{2}$$

we have

$$\left(D_w + D_e + D_n + D_s + \frac{F_w}{2} - \frac{F_e}{2} + \frac{F_n}{2} - \frac{F_s}{2} \right) \phi_P =$$

$$\left(D_w - \frac{F_w}{2} \right) \phi_W + \left(D_e + \frac{F_e}{2} \right) \phi_E + \left(D_n - \frac{F_n}{2} \right) \phi_N + \left(D_s + \frac{F_s}{2} \right) \phi_S + S \cdot r \cdot \Delta r \cdot \Delta \theta$$

This can be generalized as

$$a_P \phi_P = a_W \phi_W + a_E \phi_E + a_N \phi_N + a_S \phi_S + b \quad (\text{C.7})$$

where

$$a_W = D_w - \frac{F_w}{2}$$

$$a_E = D_e + \frac{F_e}{2}$$

$$a_N = D_n - \frac{F_n}{2}$$

$$a_S = D_s + \frac{F_s}{2}$$

$$a_P = a_W + a_E + a_N + a_S - \frac{F_w}{2} + \frac{F_e}{2} - \frac{F_n}{2} + \frac{F_s}{2}$$

$$b = S \cdot r \cdot \Delta r \cdot \Delta \theta \quad (\text{C.8})$$

Upwind Differencing Scheme

Let

$$\phi_w = \begin{cases} \phi_P, & \text{if } F_w > 0 \\ \phi_W, & \text{if } F_w < 0 \end{cases}, \quad \phi_e = \begin{cases} \phi_P, & \text{if } F_e > 0 \\ \phi_E, & \text{if } F_e < 0 \end{cases}$$

$$\phi_n = \begin{cases} \phi_P, & \text{if } F_n > 0 \\ \phi_N, & \text{if } F_n < 0 \end{cases}, \quad \phi_s = \begin{cases} \phi_P, & \text{if } F_s > 0 \\ \phi_S, & \text{if } F_s < 0 \end{cases}$$

we have

$$\begin{aligned}
a_W &= D_w + \max\{-F_w, 0\} \\
a_E &= D_e + \max\{F_e, 0\} \\
a_N &= D_n + \max\{-F_n, 0\} \\
a_S &= D_s + \max\{F_s, 0\} \\
a_P &= a_W + a_E + a_N + a_S \\
b &= S \cdot r \cdot \Delta r \cdot \Delta \theta
\end{aligned}
\tag{C.9}$$

The coefficients of the discretized equation can be generalized for various schemes:

$$\begin{aligned}
a_W &= D_w A(|P_w|) + \max\{-F_w, 0\} \\
a_E &= D_e A(|P_e|) + \max\{F_e, 0\} \\
a_N &= D_n A(|P_n|) + \max\{-F_n, 0\} \\
a_S &= D_s A(|P_s|) + \max\{F_s, 0\}
\end{aligned}
\tag{C.10}$$

where $P = F / D$ (Peclet Number) and the function $A(|P|)$ is listed the following table.

Table C.1 Function $A(|P|)$ for different schemes

Schemes	$A(P)$
Central differencing	$1 - 0.5 P $
Upwind differencing	1
Power law	$\max\{0, (1 - 0.1 P)^5\}$
Hybrid	$\max\{0, 1 - 0.5 P \}$

Appendix D. Convective, Diffusive, and Source Terms

For the stream function ψ :

$$F_e = F_w = F_n = F_s = 0 \quad (\text{no convective terms})$$

$$D_n = \frac{r_n \Delta\theta}{(\delta r)_n} = (j + 0.5)\Delta\theta$$

$$D_s = \frac{r_s \Delta\theta}{(\delta r)_s} = (j - 0.5)\Delta\theta$$

$$D_e = \frac{\Delta r}{r_e (\delta\theta)_e} = \frac{1}{\Delta\theta} \ln \frac{j + 0.5}{j - 0.5}$$

$$D_w = \frac{\Delta r}{r_w (\delta\theta)_w} = \frac{1}{\Delta\theta} \ln \frac{j + 0.5}{j - 0.5}$$

The convective terms for \hat{w} and ζ are:

$$F_e = \left(-\frac{\partial\psi}{\partial r} \right)_e \Delta r = -\frac{1}{4} (\psi_{i-1,j+1} + \psi_{i,j+1} - \psi_{i-1,j-1} - \psi_{i,j-1})$$

$$F_w = \left(-\frac{\partial\psi}{\partial r} \right)_w \Delta r = -\frac{1}{4} (\psi_{i,j+1} + \psi_{i+1,j+1} - \psi_{i,j-1} - \psi_{i+1,j-1})$$

$$F_n = \left(\frac{\partial\psi}{\partial\theta} \right)_n \Delta\theta = \frac{1}{4} (\psi_{i+1,j+1} + \psi_{i+1,j} - \psi_{i-1,j} - \psi_{i-1,j+1})$$

$$F_s = \left(\frac{\partial\psi}{\partial\theta} \right)_s \Delta\theta = \frac{1}{4} (\psi_{i+1,j} + \psi_{i+1,j-1} - \psi_{i-1,j} - \psi_{i-1,j-1})$$

The convective term for T is:

$$F_e = \left(-\text{Pr} \frac{\partial\psi}{\partial r} \right)_e \Delta r = -\frac{\text{Pr}}{4} (\psi_{i-1,j+1} + \psi_{i,j+1} - \psi_{i-1,j-1} - \psi_{i,j-1})$$

$$F_w = \left(-\text{Pr} \frac{\partial\psi}{\partial r} \right)_w \Delta r = -\frac{\text{Pr}}{4} (\psi_{i,j+1} + \psi_{i+1,j+1} - \psi_{i,j-1} - \psi_{i+1,j-1})$$

$$F_n = \left(\text{Pr} \frac{\partial \psi}{\partial \theta} \right)_n \Delta \theta = \frac{\text{Pr}}{4} (\psi_{i+1,j+1} + \psi_{i+1,j} - \psi_{i-1,j} - \psi_{i-1,j+1})$$

$$F_s = \left(\text{Pr} \frac{\partial \psi}{\partial \theta} \right)_s \Delta \theta = \frac{\text{Pr}}{4} (\psi_{i+1,j} + \psi_{i+1,j-1} - \psi_{i-1,j} - \psi_{i-1,j-1})$$

The diffusive terms for \hat{w} , ζ and T are:

$$D_n = \frac{r_n \Delta \theta}{(\delta r)_n} = (j + 0.5) \Delta \theta$$

$$D_s = \frac{r_s \Delta \theta}{(\delta r)_s} = (j - 0.5) \Delta \theta$$

$$D_e = \frac{r_e \left[\frac{1}{r_e^2} + \left(\frac{\pi}{2y} \right)^2 \right] \Delta r}{(\delta \theta)_e} = \left[\ln \frac{j + 0.5}{j - 0.5} + j \left(\frac{\pi}{2y} \Delta r \right)^2 \right] / \Delta \theta$$

$$D_w = \frac{r_w \left[\frac{1}{r_w^2} + \left(\frac{\pi}{2y} \right)^2 \right] \Delta r}{(\delta \theta)_w} = \left[\ln \frac{j + 0.5}{j - 0.5} + j \left(\frac{\pi}{2y} \Delta r \right)^2 \right] / \Delta \theta$$

The source terms for \hat{w} , ψ , ζ and T are:

Axial velocity: $S_{i,j} = 1$

Stream function: $S_{i,j} = \frac{\pi r_{i,j}}{2y} \frac{w_{i,j+1} - w_{i,j-1}}{2\Delta r} + \frac{\pi w_{i,j}}{y} + \zeta_{i,j}$

Vorticity: $S_{i,j} = -\frac{\pi}{2y} \left[\frac{w_{i+1} - w_{i-1}}{2\Delta \theta} \left(\frac{\psi_{i,j+1} - 2\psi_{i,j} + \psi_{i,j-1}}{\Delta r^2} + \frac{1}{r_{i,j}} \frac{\psi_{i,j+1} - \psi_{i,j-1}}{2\Delta r} + \frac{\pi w_{i,j}}{y} \right) - \frac{w_{i,j+1} - w_{i,j-1}}{2\Delta r} \frac{\psi_{i+1,j+1} + \psi_{i-1,j-1} - \psi_{i+1,j-1} - \psi_{i-1,j+1}}{4\Delta r \Delta \theta} \right]$

Temperature: $S_{i,j} = \frac{w_{i,j}}{w_m} \frac{T_{i,j}}{T_m}$ for UWT

$S_{i,j} = \frac{w_{i,j}}{w_m}$ for UHF

Appendix E. Implementation of Boundary Conditions

All the dependent variables are zero at the boundaries except the vorticity and temperature, which needs extra treatment. Taylor series can be applied to express second order terms, but it

lacks sufficient accuracy for the first order term $\left. \frac{\partial w}{\partial r} \right|_N$. A better solution is to use third-order

interpolation, which results in

$$\left. \frac{\partial w}{\partial r} \right|_N = \frac{w_{N-2} - 4w_{N-1}}{2\Delta r}.$$

Therefore, the discretized expressions for vorticity are as follows:

$$0 < r < 1, \theta = 0 : \quad \zeta_{0,j} = -\frac{2\psi_{1,j}}{r_{0,j}^2 \Delta\theta^2}$$

$$r = 1, 0 < \theta < \pi : \quad \zeta_{i,N} = -\left[\frac{2\psi_{i,N-1}}{\Delta r^2} + \frac{\pi}{2y} \frac{w_{i,N-2} - 4w_{i,N-1}}{2\Delta r} \right]$$

$$0 < r < 1, \theta = \pi : \quad \zeta_{M,j} = -\frac{2\psi_{M-1,j}}{r_{M,j}^2 \Delta\theta^2}$$

$$r = 1, 0 \leq \theta \leq \pi : \quad \zeta_{i,0} = -\frac{2\psi_{\frac{M}{2},1}}{\Delta r^2}$$

For adiabatic tape insert, the tape surface temperature is determined by the following thermal boundary condition:

$$\left. \frac{\partial T}{\partial n} \right|_w = 0$$

Similarly, a third-order interpolation is applied to yield

$$T_0 = \frac{4T_1 - T_2}{3}$$

where T_1 and T_2 are the two adjacent points vertically above the boundary node T_0 and can be expressed in terms of the neighboring mesh points:

$$0 < r < 1, \theta = 0: \quad T_1 = T_{1,j} + (T_{1,j+1} - T_{1,j}) \left(\frac{1}{\cos \Delta \theta} - 1 \right) j$$

$$T_2 = T_{2,j} + (T_{2,j+1} - T_{2,j}) \left(\frac{1}{\cos 2 \Delta \theta} - 1 \right) j$$

$$T_{0,j} = \frac{4T_2 - T_1}{3}$$

$$0 < r < 1, \theta = \pi: \quad T_1 = T_{M-1,j} + (T_{M-1,j+1} - T_{M-1,j}) \left(\frac{1}{\cos \Delta \theta} - 1 \right) j$$

$$T_2 = T_{M-2,j} + (T_{M-2,j+1} - T_{M-2,j}) \left(\frac{1}{\cos 2 \Delta \theta} - 1 \right) j$$

$$T_{M,j} = \frac{4T_2 - T_1}{3}$$

$$r = 0, \quad 0 \leq \theta \leq \pi: \quad T_{i,0} = \frac{4T_{\frac{M}{2},1} - T_{\frac{M}{2},2}}{3}$$